Doping- and strain-tuned high Curie temperature half-metallicity and quantum anomalous Hall effect in monolayer $NiAl_2S_4$ with non-Dirac and Dirac states

Yujie Wang,[1] Chenchen Lou,[1] Bao Zhao,[2] Chunlan Ma,[1] and Jiayong Zhang[1,*]

[1]*Jiangsu Key Laboratory of Micro and Nano Heat Fluid Flow Technology and Energy Application, School of Physical Science and Technology, Suzhou University of Science and Technology, Suzhou 215009, China*

[2]*School of Physics Science and Information Technology, Shandong Key Laboratory of Optical Communication Science and Technology, Liaocheng University, Liaocheng 252059, China*

(Received 20 October 2022; accepted 7 February 2023; published 15 February 2023)

Two-dimensional magnetic materials with tunable electronic and magnetic properties are promising for designing spintronics devices. Here we study, using first-principles calculations, the electronic, magnetic, and topological properties of monolayer $NiAl_2S_4$. Monolayer $NiAl_2S_4$ is in the noncollinear 120^0-antiferromagnetic (120^0-AFM) state and is an indirect band gap semiconductor. Although the 120^0-AFM state in monolayer $NiAl_2S_4$ is robust against strain, its magnetic structure can be tuned effectively by carrier doping. Remarkably, monolayer $NiAl_2S_4$ can be tuned into a high Curie temperature (T_C) half-metallic state by hole doping. The T_C of ferromagnetic monolayer $NiAl_2S_4$ increases with hole-doping concentration and can be increased up to room temperature. For the hole-doped monolayer $NiAl_2S_4$ with the half-metallic state, before the spin-orbit coupling (SOC) is included, the two spin-up bands around the Fermi level are simultaneously degenerate at the Γ point (dominated by S p_x/p_y states) and K/K′ points (dominated by S p_z state) with quadratic non-Dirac and linear Dirac band dispersions, respectively. When the SOC is included, topologically nontrivial gaps with Chern number $C = 1$ will be opened, respectively, around the non-Dirac Γ point and Dirac K/K′ points. More interestingly, the quantum anomalous Hall (QAH) effect with high Chern number $C = 2$ can be achieved in the tensile-strained monolayer $NiAl_2S_4$ with 1.0 hole-doped per unit cell. The obtained high Chern number of $C = 2$ results from the constructive coupling effect between the topological nontrivial non-Dirac and Dirac states, which is analyzed through a schematic depiction. Our results show that monolayer $NiAl_2S_4$ is a promising candidate for the exploration of high T_C spintronics devices and high Chern number QAH effect.

DOI: 10.1103/PhysRevB.107.085416

I. INTRODUCTION

Since the discovery of graphene, two-dimensional (2D) materials have attracted enormous attention due to their potential applications in high-performance low-dimensional electronics and spintronics devices. 2D materials possess lots of physical properties, such as topological quantum state in graphene [1], high-temperature quantum spin Hall (QSH) effect in bismuthene [2], and valley Hall effect in transition metal (TM) dichalcogenides MX_2 (TMDs) [3]. Most of the 2D materials are nonmagnetic, such as graphene [4], h-BN [5], and TMDs [6]. In recent years, 2D magnetic materials have become research hot spots in condensed matter physics and material science because of their rich physics in 2D magnetism and spintronics. For magnetic metals, the half metal, proposed by de Groot *et al.* [7], is a kind of important spintronics material that can intrinsically provide single spin channel electrons (with 100% spin polarization) due to its metallicity for one spin channel and insulating or semiconducting for the other spin channel. For magnetic semiconductors, the bipolar ferromagnetic (FM) semiconductor [8] and half semiconductor [9] are two kinds of ideal spintronics materials. Up to now, several kinds of 2D monolayer magnetic materials have been theoretically proposed, such as monolayer TM trichalcogenide $CrGeTe_3$ [10,11] in the FM state, monolayer $MnPX_3$ (X = S, Se) [11] in the Néel antiferromagnetic (AFM-Néel) state, and monolayer TM trihalides MX_3 (M = TM atom, X = Cl, Br, I) [12–17] in the FM state. Remarkably, monolayer CrI_3 [18] and bilayer $Cr_2Ge_2Te_6$ [19] have been successfully synthesized in experiments and proved to be 2D FM semiconductors. Sivadas *et al.* [11] showed that strain can be an effective knob for tuning the magnetic properties of monolayer ABX_3. Wang *et al.* [20] predicted that the room-temperature FM half metallicity could be achieved in monolayer CrI_3 via hole doping. Zhang *et al.* [21] predicted that the magnetic ground state of monolayer MoX_3 (X = Cl, Br, I) could be tuned by strain and carrier doping. Li *et al.* [22] predicted that both electron and hole doping can induce monolayer $MnPSe_3$ transitions from AFM semiconductors to FM half metals. Therefore, strain and carrier doping are the two effective ways to regulate the magnetic structures and spintronics properties of 2D magnetic materials.

2D FM materials with high Curie temperature and suitable band structures are promising for achieving the quantum anomalous Hall (QAH) effect. The QAH state is insulating in bulk but exhibits robust conducting edge states that are topologically protected from backscattering and leading to

*jyzhang@usts.edu.cn

quantized Hall conductivity without the need of an external magnetic field [23–25]. The realization of the QAH effect in realistic materials is of great significant due to its great potential applications in low-power-consumption electronic devices. During recent years, the QAH effect has been theoretically predicted to occur in some 2D material systems, such as TM atom-doped topological insulator thin films [26], graphene- and silicene-based systems [27–32], 2D monolayer metal-organic frameworks [33,34], monolayer TM trihalides MX_3 [13–16], monolayer TM oxides [35], layered $MnBi_2Te_4$-family materials [36,37], and so on. The QAH effect has been experimentally realized in TM atom-doped $(Bi,Sb)_2Te_3$ thin films [38,39] and layered $MnBi_2Te_4$ [40], significantly promoting the development of this important research field. Up to the present, several different strategies have been proposed to generate the QAH effect. Qiao *et al.* [27] showed that the QAH state can be realized in the Dirac bands by introducing both magnetic exchange field and Rashba spin-orbit coupling (SOC). For the fully spin-polarized Dirac bands [33], the SOC can open a topologically nontrivial gap at the degenerate Dirac K/K′ points and induce the QAH state with $C_{\mathrm{Dirac}} = C_{\mathrm{K}} + C_{\mathrm{K'}} = \pm 1$. For the 2D magnetic material system with a small band gap, according to the Bernevig-Hughes-Zhang model [41], the QAH state can be obtained if the SOC-induced band inversion only happens in one spin state (spin-up or spin-down state). For the non-Dirac bands, theoretical studies [42–45] show that the SOC-induced energy gap around the fully spin-polarized degenerate Γ point with non-Dirac band dispersions is the QAH state with $C_{\mathrm{non-Dirac}} = C_{\Gamma} = \pm 1$. If the fully spin-polarized energy degenerate Dirac K/K′ points and non-Dirac Γ point simultaneously exist before SOC is included, the topologically trivial state with $C = 0$ (due to the destructive coupling effect [43]) or high Chern number QAH state with $C = \pm 2$ (due to the constructive coupling effect [45]) could be obtained when SOC is considered.

In this paper, we systematically study the electronic structures, magnetic properties, and topological properties of monolayer $NiAl_2S_4$ by using first-principles calculations. The stabilities of the monolayer $NiAl_2S_4$ are confirmed by the formation energy calculations, phonon spectrum calculations, and *ab initio* molecular dynamic (AIMD) simulations. The calculation results show that the monolayer $NiAl_2S_4$ is in the noncollinear 120^0-antiferromagnetic (120^0-AFM) state and is a semiconductor with an indirect band gap of 1.52 eV. The magnetic properties of monolayer $NiAl_2S_4$ with respect to strain and carrier doping are explored, from which we can find that the obtained 120^0-AFM state is robust against strain and the magnetic structures of monolayer $NiAl_2S_4$ can be tuned effectively by carrier doping. The obtained magnetic phase diagrams with respect to carrier doping concentrations show that the FM state can be achieved in monolayer $NiAl_2S_4$ and the Curie temperature (T_C) increases with the increase of hole doping concentration. In addition, the FM state in hole-doped monolayer $NiAl_2S_4$ is robust against strain. The calculated band structures and density of states (DOS) demonstrate that the hole-doped monolayer $NiAl_2S_4$ in FM states are half metals and the room-temperature FM half-metallic state can be realized. The magnetic anisotropy energy (MAE) of hole-doped monolayer $NiAl_2S_4$ can be tuned by hole-doping concentration and strain. For the hole-doped monolayer $NiAl_2S_4$ with the half-metallic state, the two spin-up bands around the Fermi level (E_{F}) are simultaneously degenerate at the Γ point and K/K′ points with quadratic non-Dirac and linear Dirac band dispersions, respectively. The non-Dirac bands at Γ point and Dirac bands at K/K′ points are dominated by S p_x/p_y states and S p_z state, respectively. The QAH effect with a high Chern number of $C = 2$ can be achieved in tensile-strained monolayer $NiAl_2S_4$ with the carrier doping concentration of 1.0 holes per unit cell.

II. COMPUTATIONAL DETAILS

The first-principles calculations are performed by using the projected augmented wave [46] formalism based on density functional theory (DFT), as implemented in the VIENNA AB INITIO SIMULATION PACKAGE (VASP) [47]. The Perdew-Burke-Ernzerhof generalized gradient approximation (GGA-PBE) is employed to describe the exchange and correlation functional [48]. The GGA+U method [49] is adopted to describe the correlation effects of the Ni 3d electrons. The values of the on-site Coulomb interaction U and exchange interaction J are set to be 4.0 eV and 1.0 eV, respectively. The energy cutoff of the plane-wave and the convergence criteria of the total energy are set to be 550 eV and 10^{-6} eV, respectively. A vacuum space of about 18 Å is used to avoid any interaction between adjacent slabs. All atoms in the unit cell are allowed to relax until the Hellmann-Feynman force on each atom is smaller than 0.01 eV/Å. The $18 \times 18 \times 1$, $9 \times 18 \times 1$, and $9 \times 9 \times 1$ gamma central Monkhorst-Pack grids are adopted during the calculations for the $1 \times 1 \times 1$ unit cell, $2 \times 1 \times 1$ supercell, and $\sqrt{3} \times \sqrt{3} \times 1$ supercell of the monolayer $NiAl_2S_4$. The GGA-PBE method is adopted to calculate the lattice constant of monolayer $NiAl_2S_4$. The phonon spectrum is calculated by using the density functional perturbation theory (DFPT) method as implemented in the PHONOPY code [50] combined with VASP. The AIMD simulation with a $3 \times 3 \times 1$ supercell at 500 K is performed to investigate the thermal stability. The Monte Carlo (MC) simulations based on the classical 2D Heisenberg model are performed to estimate the Curie temperature. The maximally localized Wannier functions (MLWFs) [51,52] are constructed by using the WANNIER90 package [53], and the Berry curvatures and Chern numbers are calculated by employing the algorithm described in Ref. [54]. The DOS of the semi-infinite system is calculated by using the WANNIERTOOLS package [55].

III. RESULTS AND DISCUSSION

A. Crystal structure and stabilities

Bulk AB_2M_4 (A = TM atom; B = Al, Ga, In; M = S, Se) [56] are layered materials with each monolayer bonded by van der Waals interactions. Thus, in principle, 2D monolayer AB_2M_4 can be exfoliated from its bulk phases. Here, the considered crystal structure of AB_2M_4 has space group $P\bar{3}m1$ (No. 164), and we predict that monolayer $NiAl_2S_4$ is a unique 2D material with the same crystal structure as bulk AB_2M_4 [56]. The crystal structure of monolayer $NiAl_2S_4$, as depicted in Figs. 1(a) and 1(b), consists of seven atomic layers, where the Ni atomic layer is in the middle of the monolayer structure and

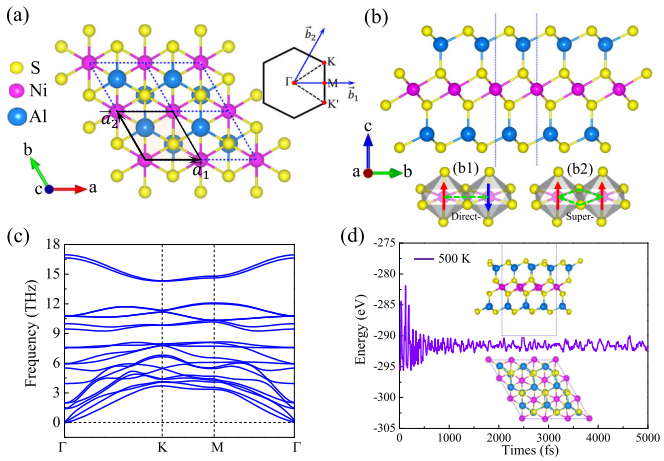

FIG. 1. (a), (b) Top and side views of the atomic structure of monolayer $NiAl_2S_4$. The rhombus in (a) shows the unit cell with lattice vectors $\vec{a}_1$ and $\vec{a}_2$. The inset in (a) shows the first Brillouin zone with high symmetry points. The bottom insets in (b) show the sulfur octahedron. (b1) Schematic plot of the direct exchange coupling of Ni − Ni. (b2) Schematic plot of the superexchange coupling of Ni − S − Ni. (c) The calculated phonon spectrum for the monolayer $NiAl_2S_4$. (d) The fluctuation of total energies of the monolayer $NiAl_2S_4$ system with respect to time during AIMD simulations at 500 K. The insets in (d) show the top and side views of atomic configuration snapshots from AIMD simulations after 5.0 ps.

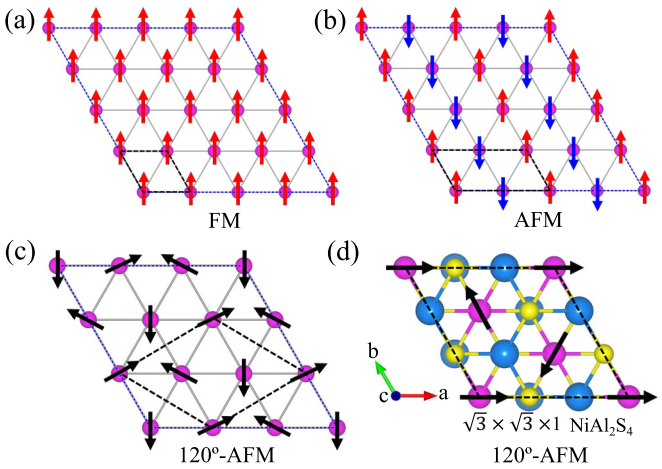

FIG. 2. (a)–(c) The three typical magnetic configurations of the 2D triangular lattice: FM (a), collinear AFM (b), and noncollinear 120^0-AFM (c). (d) The $\sqrt{3} \times \sqrt{3} \times 1$ supercell of $NiAl_2S_4$ monolayer with the noncollinear 120^0-AFM magnetic configuration. The red and blue arrows in (a) and (b) denote the collinear up and down spins. The black arrows in (c) and (d) denote the noncollinear spins that lie in the 2D plane.

is sandwiched between two S-Al-S atomic layers. The unit cell of monolayer $NiAl_2S_4$ with lattice vectors $\vec{a}_1$ and $\vec{a}_2$ is denoted in Fig. 1(a). The unit cell contains one Ni atom, two Al atoms, and four S atoms, where the Ni atoms form a 2D triangular lattice. The optimized equilibrium lattice constant of the monolayer $NiAl_2S_4$ obtained by using the GGA-PBE functional is $a = 3.63$ Å. The first Brillouin zone (BZ) with reciprocal lattice vectors $\vec{b}_1$ and $\vec{b}_2$ and the high symmetry points Γ, M, K, and K′ are given in the inset in Fig. 1(a).

The structural stabilities of the monolayer $NiAl_2S_4$ are examined by the formation energy calculations, phonon spectrum calculations, and AIMD simulations. The formation energy of monolayer $NiAl_2S_4$ is defined as $E_{\text{form}} = E(\text{NiAl}_2\text{S}_4) - \text{E(Ni)} - 2\text{E(Al)} - \text{E(S)}/8$, where $E(\text{NiAl}_2\text{S}_4)$ is the total energy of the monolayer $NiAl_2S_4$ unit cell, $E(\text{Ni})$ is the total energy of bulk Ni in the face-centered cubic unit cell with one Ni atom, $E(\text{Al})$ is the total energy of bulk Al in the face-centered cubic unit cell with one Al atom, and $E(\text{S})$ is the total energy of bulk S containing four S_8 rings (32 S atoms) in the calculated cell. The calculated formation energies for the monolayer $NiAl_2S_4$ by using the GGA and GGA + U functional are −6.18 eV and −5.46 eV, respectively. The obtained large negative values of the formation energy indicate that monolayer $NiAl_2S_4$ will form a strongly bonded network, guaranteeing the feasibility of the experimental synthesis of this 2D material. To further examine the dynamical and thermal stabilities of the monolayer $NiAl_2S_4$, phonon spectrum calculations and AIMD simulations are carried out. The calculated phonon spectrum is shown in Fig. 1(c), from which we can find that there is no imaginary-frequency mode in the whole BZ, indicating the dynamical stability of the monolayer $NiAl_2S_4$. Figure 1(d) shows the fluctuation of total energies of the monolayer $NiAl_2S_4$ system with respect to time during AIMD simulations at 500 K. The top and side views of atomic configuration snapshots from the AIMD simulations after 5.0 ps at 500 K are given in the insets in Fig. 1(d), from which we can find that monolayer $NiAl_2S_4$ can maintain its structural integrity, indicating the thermal stability of the monolayer $NiAl_2S_4$. According to the calculated formation energy, phonon spectrum, and AIMD simulations, the crystal structure of monolayer $NiAl_2S_4$ is dynamically and thermally stable at room temperature.

B. Magnetic properties and hole doping induced FM state

To investigate the magnetic properties of the monolayer $NiAl_2S_4$, we consider the following three typical magnetic configurations of the 2D triangular lattice: FM, collinear AFM, and noncollinear 120^0-AFM, as shown in Figs. 2(a)–2(c). The total energies of the FM, collinear AFM, and noncollinear 120^0-AFM states of the monolayer $NiAl_2S_4$ are calculated with the $1 \times 1 \times 1$ unit cell, $2 \times 1 \times 1$ supercell, and $\sqrt{3} \times \sqrt{3} \times 1$ supercell, respectively. The $\sqrt{3} \times \sqrt{3} \times 1$ supercell of monolayer $NiAl_2S_4$ with three Ni atoms is the minimum calculated cell for the noncollinear 120^0-AFM state, as illustrated in Fig. 2(d). To compare the energy difference between the considered three magnetic configurations, the obtained total energies of the FM, collinear AFM, and noncollinear 120^0-AFM states are divided by one, two, and three, respectively. The energy difference (ΔE) between AFM and FM states ($E_{\text{AFM}} - E_{\text{FM}}$) and noncollinear 120^0-AFM and FM states ($E_{120^0-\text{AFM}} - E_{\text{FM}}$) for monolayer $NiAl_2S_4$ are 2.2 meV and −6.3 meV, respectively, indicating that the magnetic ground state of monolayer $NiAl_2S_4$ is the noncollinear 120^0-AFM state, as shown in Fig. 3(a). The obtained energy difference ΔE in Fig. S16 in the Supplemental Material [57] illustrates that the magnetic ground state of monolayer

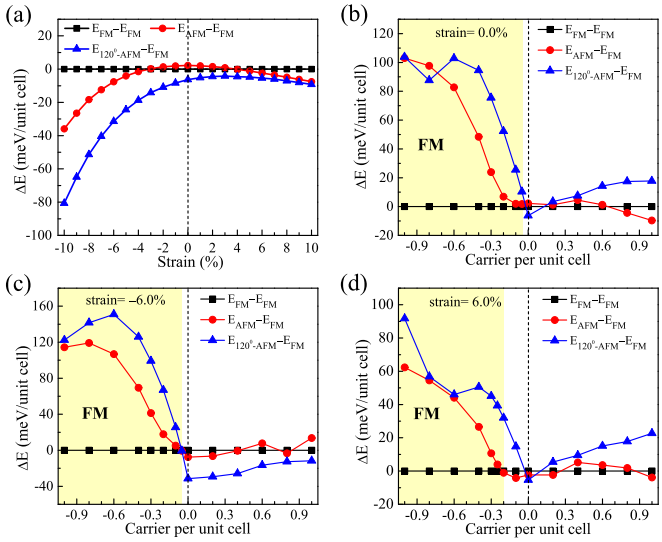

FIG. 3. (a) The energy difference (ΔE) between FM and FM state ($E_{\mathrm{FM}} - E_{\mathrm{FM}}$), AFM and FM state ($E_{\mathrm{AFM}} - E_{\mathrm{FM}}$), and noncollinear 120^0-AFM and FM state ($E_{120^0-\mathrm{AFM}} - E_{\mathrm{FM}}$) as a function of strain for monolayer $NiAl_2S_4$. (b)–(d) The calculated ΔE of $E_{\mathrm{FM}} - E_{\mathrm{FM}}$, $E_{\mathrm{AFM}} - E_{\mathrm{FM}}$, and $E_{120^0-\mathrm{AFM}} - E_{\mathrm{FM}}$ as a function of carrier concentration for the 0.0% strained (b), 6.0% compressive strained (c), and 6.0% tensile-strained (d) monolayer $NiAl_2S_4$.

$NiAl_2S_4$ is robust against effective Hubbard U (0.0 − 5.0 eV). For the FM state monolayer $NiAl_2S_4$, the total magnetic moment is 2.0 μ_B per unit cell and is mainly contributed by Ni atom. Here, we apply biaxial compressive and tensile strain. The strain is defined as $(a - a_0)/a_0 \times 100\%$, where a stands for the lattice constant with strain applied and a_0 strands for the equilibrium lattice constant. Figure 3(a) shows the energy differences (ΔE) of $E_{\mathrm{FM}} - E_{\mathrm{FM}}$, $E_{\mathrm{AFM}} - E_{\mathrm{FM}}$, and $E_{120^0-\mathrm{AFM}} - E_{\mathrm{FM}}$ as a function of strain for monolayer $NiAl_2S_4$, from which we can find that both $E_{\mathrm{AFM}} - E_{\mathrm{FM}}$ and $E_{120^0-\mathrm{AFM}} - E_{\mathrm{FM}}$ decrease rapidly with the increase of compressive strain, indicating that the noncollinear 120^0-AFM state will become more stable in monolayer $NiAl_2S_4$ by applying compressive strain. The energy difference of $E_{120^0-\mathrm{AFM}} - E_{\mathrm{FM}}$ in monolayer $NiAl_2S_4$ can be decreased to −24.4 meV and −51.4 meV by applying 5.0% and 8.0% compressive strain, respectively, as illustrated in Fig. 3(a). When the tensile strain is applied, the ΔE will not change significantly. Figure 3(a) illustrates that the obtained magnetic ground state of the noncollinear 120^0-AFM state in monolayer $NiAl_2S_4$ is robust against strain.

The Ni atoms in monolayer $NiAl_2S_4$ are surrounded by six nearest-neighbor (NN) S atoms, forming the sulfur octahedron structure, as illustrated in Fig. 1(b). The mechanism of the magnetic states in monolayer $NiAl_2S_4$ can be understood from the competition between the direct exchange and superexchange interactions. The direct exchange comes from direct electron hopping between the NN Ni-Ni sites. Since the distance between NN Ni atoms is not very large, the direct exchange interaction between the two NN Ni atoms cannot be neglected, which leads to the AFM arrangement of the two Ni atoms [Fig. 1(b1)]. The superexchange interaction is mediated through the S atoms. Due to the Ni-S-Ni angle (97.0^0) being close to 90^0 in the superexchange path shown in Fig. 1(b2), according to the Goodenough rule [58,59], the superexchange interaction is expected to be FM. For the monolayer $NiAl_2S_4$, the direct exchange interaction is dominant. When applying the compressive strain and tensile strain, the strength of the superexchange FM interaction will be slightly enhanced and weakened, respectively, due to the Ni-S-Ni angle not changing much. The strength of the direct exchange AFM interaction will be weakened slightly when applying the tensile strain. The strength of the direct exchange AFM interaction will be enhanced rapidly with the increase of compressive strain due to the decrease of the NN Ni atoms distance. Thus, the obtained energy difference ΔE in Fig. 3(a) is insensitive to tensile strain while depending strongly on compressive strain.

Previous studies show that carrier doping is an effective way of tuning the magnetic structures and critical temperatures of the 2D monolayer magnetic materials, such as CrI_3 [20], VCl_3 [17], MoX_3 [21], and $MnPSe_3$ [22]. Therefore, we systematically investigate the magnetic properties of the monolayer $NiAl_2S_4$ with the variation of carrier doping concentrations. The three typical magnetic configurations of FM, collinear AFM, and noncollinear 120^0-AFM are considered. The total energies of the three different magnetic configurations for the carrier-doped monolayer $NiAl_2S_4$ are calculated by adding or removing some electrons from the calculated cell and neutralizing the system with a homogeneous charge background. The carrier density up to $\sim 10^{15}$ cm^{-2} has already been achieved in experiments [60,61]. In our calculations, the maximum carrier doping concentrations of 1.0 holes or 1.0 electrons per unit cell are considered. The corresponding maximum doping concentration is 8.77×10^{14} cm^{-2}, which can be experimentally realized through currently advanced gating technologies. Figure 3(b) shows the calculated energy differences of $E_{\mathrm{FM}} - E_{\mathrm{FM}}$, $E_{\mathrm{AFM}} - E_{\mathrm{FM}}$, and $E_{120^0-\mathrm{AFM}} - E_{\mathrm{FM}}$ as a function of carrier doping concentration for the monolayer $NiAl_2S_4$. The energy differences of $E_{\mathrm{AFM}} - E_{\mathrm{FM}}$ ($E_{120^0-\mathrm{AFM}} - E_{\mathrm{FM}}$) for monolayer $NiAl_2S_4$ with carrier doping concentrations of 0.2 holes and 0.6 holes per unit cell are 6.8 meV (52.3 meV) and 82.7 meV (102.9 meV), respectively, indicating that the magnetic structure of monolayer $NiAl_2S_4$ could be tuned from 120^0-AFM state to FM state by hole doping. Our calculations show that the magnetic phase transition from 120^0-AFM state to FM state can be triggered in monolayer $NiAl_2S_4$ when the hole doping concentration is greater than 0.02 holes per unit cell, which could be easily realized in experiments.

From Fig. 3(b), we can observe that the total energy of the 120^0-AFM state is much higher than the collinear AFM state within the same hole doping concentration. In addition, $E_{\mathrm{AFM}} - E_{\mathrm{FM}}$ increased rapidly when the hole doping concentration is greater than 0.1 holes per unit cell, indicating that the FM state will become more stable in monolayer $NiAl_2S_4$ by increasing the hole doping concentration. Figures 3(c) and 3(d) show the calculated energy differences of $E_{\mathrm{FM}} - E_{\mathrm{FM}}$, $E_{\mathrm{AFM}} - E_{\mathrm{FM}}$, and $E_{120^0-\mathrm{AFM}} - E_{\mathrm{FM}}$ as a function of carrier doping concentration for the 6.0% compressive strained and 6.0% tensile-strained monolayer $NiAl_2S_4$, respectively, from which we can observe that the hole doping induced FM state still happens in strained monolayer $NiAl_2S_4$, indicating that

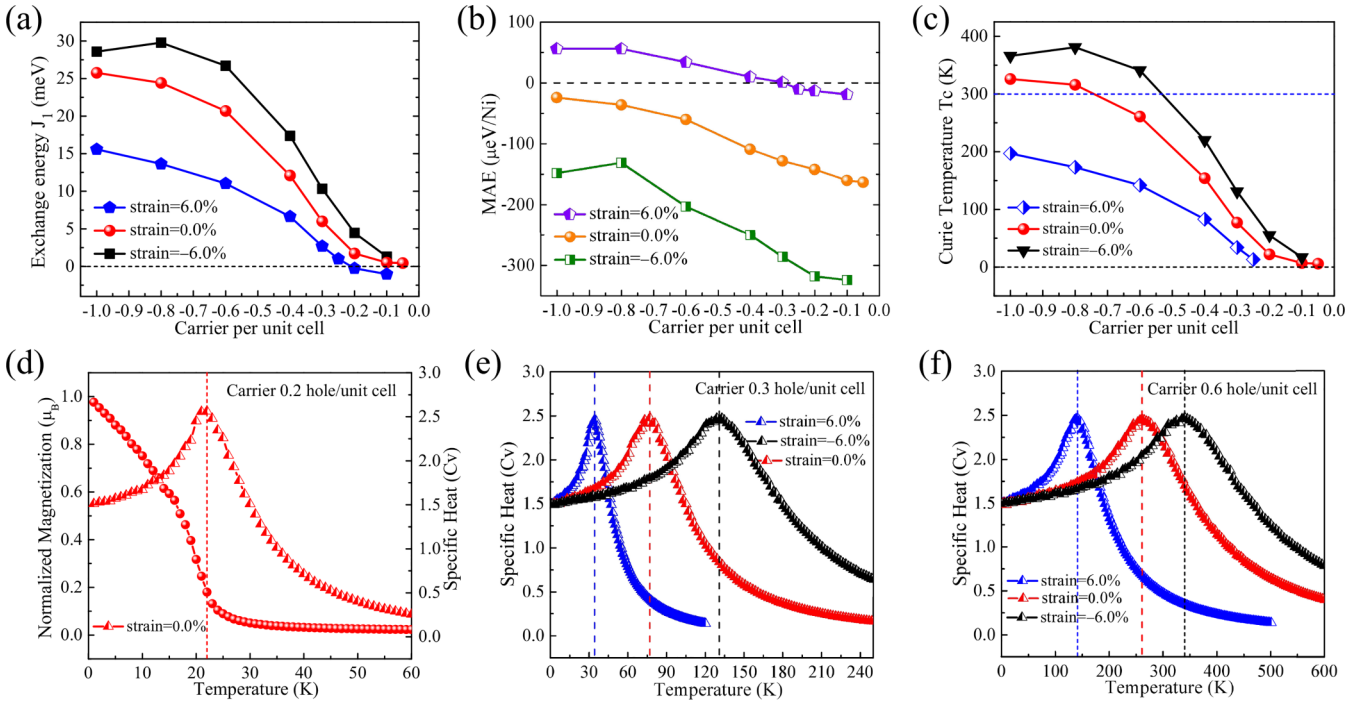

FIG. 4. (a)–(c) The calculated exchange interaction energy J_1 (a), magnetic anisotropy energy MAE (b), and Curie temperature T_C (c) as a function of carrier concentration for the 6.0% compressive strained, 0.0% strained, and 6.0% tensile-strained monolayer $NiAl_2S_4$. (d) Temperature dependence of the normalized magnetic moment and special heat capacity of the monolayer $NiAl_2S_4$ with the carrier doping concentration of 0.2 holes per unit cell. (e), (f) The special heat capacities as a function of temperature for the 6.0% compressive strained, 0.0% strained, and 6.0% tensile-strained monolayer $NiAl_2S_4$ with the carrier doping concentration of 0.3 holes (e) and 0.6 holes (f) per unit cell.

the FM state obtained in the hole-doped monolayer $NiAl_2S_4$ is robust against strain. The valence bands and conduction bands of the monolayer $NiAl_2S_4$ are mainly contributed by the S p and Ni d orbitals, respectively. For hole doping, the carrier is mainly provided by S p states; the strength of the superexchange FM interaction will be enhanced rapidly with the increase of the hole doping concentrations, while the direct exchange AFM interaction does not change much, which leads to the magnetic ground state transition from 120^0-AFM to FM state. For electron doping, the carrier is mainly provided by Ni d states; the strength of the direct exchange AFM and superexchange FM interaction will not change much. Thus, the obtained energy difference ΔE in Figs. 3(b)–3(d) is insensitive to electron doping while depending strongly on hole doping. The energy differences of $E_{AFM} - E_{FM}$ for 0.0% strained, 6.0% compressive strained, and 6.0% tensile-strained monolayer $NiAl_2S_4$ with carrier doping concentrations of 0.4 holes per unit cell are 48.4 meV, 69.5 meV, and 26.5 meV, respectively, showing that the application of compressive strain and tensile strain could respectively improve and reduce the stability of the obtained FM state in hole-doped monolayer $NiAl_2S_4$. Figure 3(d) shows that the FM state can be achieved in 6.0% tensile-strained monolayer $NiAl_2S_4$ when the carrier doping concentration is greater than 0.21 holes per unit cell, while the collinear AFM state is obtained within a small hole doping concentration.

The MAE is an important parameter for 2D magnetic materials with FM state. The MAE per Ni atom for the hole-doped monolayer $NiAl_2S_4$ with FM state is calculated through $\mathrm{MAE} = E_{[100]} - E_{[001]}$, where $E_{[100]}$ and $E_{[001]}$ are the total energies of the FM state monolayer $NiAl_2S_4$ with the magnetization along the [100] and [001] directions, respectively. The [100] and [001] directions are parallel and perpendicular to the 2D monolayer plane, respectively. We take the 6.0% tensile-strained monolayer $NiAl_2S_4$ with the carrier doping concentration of 0.6 holes per unit cell as an example to test the convergence of MAE versus k-points. The calculated MAEs in Fig. S20 in the Supplemental Material [57] show that the numerical fluctuation of the MAE is relatively small when the k-point mesh is larger than $18 \times 18 \times 1$. In this paper, the k-point mesh of $25 \times 25 \times 1$ is adopted in the calculation of MAE. The calculated MAEs for the 0.0% strained monolayer $NiAl_2S_4$ with carrier doping concentrations of 0.05 holes, 0.3 holes, and 0.6 holes per unit cell are −163.5, −128.0, and −60.3 μeV/Ni, respectively. The obtained negative values of MAE (MAE < 0) indicate that the easy axis of the hole-doped 0.0% strained monolayer $NiAl_2S_4$ is in-plane direction. Figure 4(b) shows the calculated MAE as a function of carrier concentration for the 6.0% compressive strained, 0.0% strained, and 6.0% tensile-strained monolayer $NiAl_2S_4$. The obtained MAEs for 6.0% compressive strained monolayer $NiAl_2S_4$ with carrier doping concentrations of 0.3 holes and 0.6 holes per unit cell are −286.3 and −203.5 μeV/Ni, respectively, indicating that the easy axis of the hole-doped 6.0% compressive strained monolayer $NiAl_2S_4$ is also in-plane direction and the MAE could be enhanced significantly by applying compressive strain, as illustrated in Fig. 4(b). The absolute values of MAE for 0.0% strained and 6.0%

compressive strained monolayer $NiAl_2S_4$ will decrease with the increase of hole doping concentration. The calculated MAE for strain = 6.0% with carrier doping concentrations of 0.1 holes and 0.2 holes per unit cell in Fig. 4(b) is based on the FM state. The obtained MAEs for 6.0% tensile-strained monolayer $NiAl_2S_4$ with carrier doping concentrations of 0.25 holes and 0.6 holes per unit cell are −10.5 and 34.6 μeV/Ni, respectively, indicating that the easy axis of the hole-doped 6.0% tensile-strained monolayer $NiAl_2S_4$ can be tuned from in-plane direction to out-of-plane direction with the increase of hole doping concentration, as shown in Fig. 4(b).

For the hole-doped monolayer $NiAl_2S_4$, the NN exchange interaction parameter can be extracted by mapping the total energies of the system with two different magnetic structures [Figs. 2(a) and 2(b)] to the Heisenberg spin Hamiltonian on a 2D triangular lattice,

$$H = -J_1 \sum_{\langle ij \rangle} \vec{S}_i \cdot \vec{S}_j - D \sum_i \left|\vec{S}_i^z\right|^2, \tag{1}$$

where J_1 is the exchange interactions between NN spins, $\vec{S}_i^z$ is the spin component along the z axis and D is the uniaxial anisotropy energy. The parameters J_1 and D in Eq. (1) can be obtained from the following equations:

$$E_{\mathrm{FM}} = E_0 - 6J_1|\vec{S}|^2; E_{\mathrm{AFM}} = E_0 + 2J_1|\vec{S}|^2; D = \frac{\mathrm{MAE}}{|\vec{S}|^2}, \tag{2}$$

where E_0 is the ground state energy independent of the spin configurations. Thus, the NN exchange interaction energy $J_1 = (E_{\mathrm{AFM}} - E_{\mathrm{FM}})/(8|\vec{S}|^2)$. The E_{FM} and E_{AFM} are the calculated total energies of the hole-doped $2 \times 1 \times 1$ supercell monolayer $NiAl_2S_4$ with FM and AFM states, respectively. Here, the spin $|\vec{S}|$ is set to 1.0 ($|\vec{S}| = 1.0$). The value of J_1 is positive for FM materials, while the value of J_1 is negative for AFM materials. The calculated J_1 are positive for the 6.0% compressive strained, 0.0% strained, and 6.0% tensile-strained monolayer $NiAl_2S_4$ when the carrier doping concentrations are greater than 0.05 holes, 0.02 holes, and 0.21 holes per unit cell, respectively, as illustrated in Fig. 4(a). The calculated exchange interaction energies J_1 as a function of carrier concentration for the 6.0% compressive strained, 0.0% strained, and 6.0% tensile-strained monolayer $NiAl_2S_4$ are displayed in Fig. 4(a), showing that the J_1 increase rapidly with the increase of hole doping concentration. The obtained J_1 for the 6.0% compressive strained, 0.0% strained, and 6.0% tensile-strained monolayer $NiAl_2S_4$ with carrier doping concentrations of 0.3 holes and 0.6 holes per unit cell are 10.32 and 26.71 meV, 5.99 and 20.69 meV, and 2.68 and 11.03 meV, respectively. Therefore, the monolayer $NiAl_2S_4$ with hole doping can be tuned to the FM state, and the exchange interaction energy J_1 can be tuned effectively via hole doping and strain. Using the exchange interaction parameters J_1 and D obtained from DFT calculations, the Curie temperatures T_C for hole-doped monolayer $NiAl_2S_4$ in the FM state is estimated by MC simulations based on the classic anisotropy 2D Heisenberg model with the Metropolis algorithm, in which the $60 \times 60 \times 1$ 2D triangular lattice and 10^6 MC steps for each temperature are used. The temperature-dependent normalized magnetic moment and special heat capacity (C_V) for 0.0% strained monolayer $NiAl_2S_4$ with the carrier doping concentration of 0.2 holes per unit cell are plotted in Fig. 4(d), from which we can observe that the estimated T_C is 22 K. The red C_V curves plotted in Figs. 4(e) and 4(f) show that the T_C of the 0.0% strained hole-doped monolayer $NiAl_2S_4$ can be increased to 77 K and 261 K with the carrier doping concentrations of 0.3 holes and 0.6 holes per unit cell, respectively. The black (blue) C_V curves displayed in Figs. 4(e) and 4(f) show that the T_C of the 6.0% compressive strained (6.0% tensile-strained) monolayer $NiAl_2S_4$ with the carrier doping concentrations of 0.3 holes and 0.6 holes per unit cell are 131 K (34 K) and 341 K (142 K), respectively. Figure 4(c) plots the calculated T_C as a function of carrier concentration for the 6.0% compressive strained, 0.0% strained, and 6.0% tensile-strained monolayer $NiAl_2S_4$, showing that the T_C can be increased rapidly with the increase of hole doping concentration. Remarkably, from Fig. 4(c), we can observe that the room-temperature FM state can be achieved in hole-doped monolayer $NiAl_2S_4$.

C. Electronic structures and high Curie temperature half metallicity

Figure 5(a) shows the calculated band structure (without SOC) of the monolayer $NiAl_2S_4$ in the noncollinear 120^0-AFM magnetic ground state, showing that monolayer $NiAl_2S_4$ is a semiconductor with an indirect band gap of 1.52 eV. The band structures of monolayer $NiAl_2S_4$ with the magnetic configurations of collinear AFM and FM states are semiconductors with an indirect band gap of 1.04 and 1.09 eV, respectively, as shown in Figs. S19(a) and S19(b) in the Supplemental Material [57]. The above discussions show that the magnetic structure of monolayer $NiAl_2S_4$ could be tuned from the noncollinear 120^0-AFM state to the FM state via hole doping. Therefore, the electronic structures of the hole-doped monolayer $NiAl_2S_4$ will be different from the intrinsic monolayer $NiAl_2S_4$. Figure 5(b) plots the spin-polarized band structure of monolayer $NiAl_2S_4$ with the carrier doping concentration of 0.6 holes per unit cell, from which we can observe that the spin-up state is metallic while the spin-down state is semiconducting with a band gap of 1.67 eV, indicating it is a half metal that exhibits 100% spin polarization with spin-up conducting channel around the E_F. In consideration of the T_C of 261 K obtained in monolayer $NiAl_2S_4$ with the carrier doping concentration of 0.6 holes per unit cell, we can conclude that the high Curie temperature half-metallic state is realized in hole doped monolayer $NiAl_2S_4$ system. The corresponding DOS of Fig. 5(b) is plotted in Fig. 5(e), confirming the achievement of the half-metallic state. As illustrated in Fig. 5(e), the spin-up states around the E_F are mainly contributed by S p states; in addition, a few slight Ni d states exist around the E_F due to the hybridization between S p and Ni d states. According to the atomic crystal structures illustrated in Fig. 1(a), we can find that the monolayer $NiAl_2S_4$ has a point symmetry C_3, which will induce the Ni $3d$ orbitals to split into three groups as d_{z^2}, (d_{xy}, $d_{x^2-y^2}$), and (d_{xz}, d_{yz}), and induce the S $3p$ orbitals to split into two groups as p_z and (p_x, p_y), as clearly shown in the calculated partial density of states (PDOS) in Figs. 5(f1) and 5(f2).

A fascinating band structure can be found in the half-metallic bands in Fig. 5(b), where the two spin-up bands near

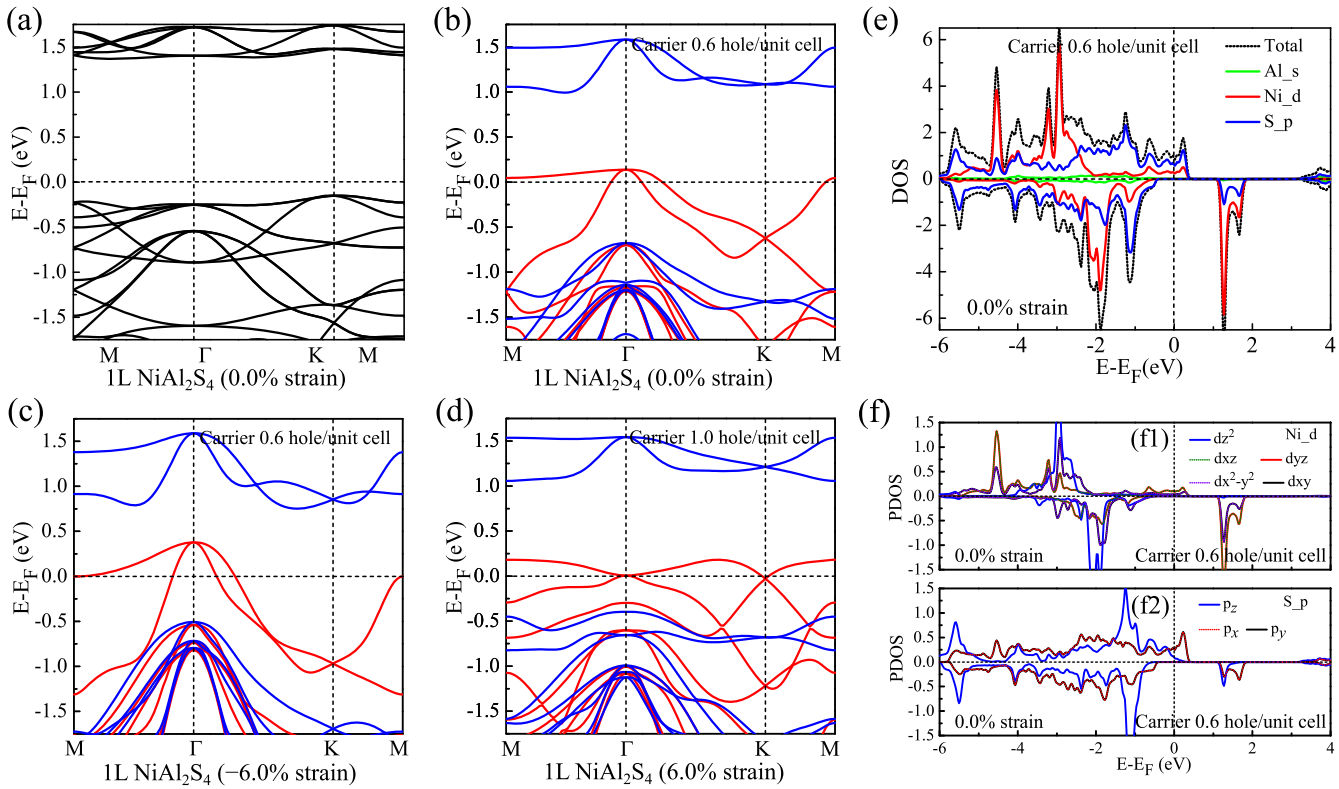

FIG. 5. (a) The band structure (without SOC) for the 0.0% strained monolayer $NiAl_2S_4$ with the noncollinear 120^0-AFM state. (b), (c) The spin-polarized band structure of the 0.0% strained (b) and 6.0% compressive strained (c) monolayer $NiAl_2S_4$ with the carrier doping concentration of 0.6 holes per unit cell. (d) The spin-polarized band structure of the 6.0% tensile-strained monolayer $NiAl_2S_4$ with the carrier doping concentration of 1.0 holes per unit cell. The red and blue curves in (b)–(d) denote the spin-up and spin-down bands, respectively. (e) The density of states (DOS) of monolayer $NiAl_2S_4$ with the carrier doping concentration of 0.6 holes per unit cell. (f) The corresponding partial density of states (PDOS) of (e).

the E_F are not only degenerate at the Γ point with quadratic non-Dirac band dispersions but also degenerate at the K/K′ points with linear Dirac band dispersions. The above interesting band structure can be seen more clearly in Fig. 6(a), which displays the magnified bands near the E_F of Fig. 5(b). According to the calculated DOS in Fig. 5(e), the two spin-up bands near the E_F in Figs. 5(b) and 6(a) are mainly contributed by the S p states. Figures 6(b) and 6(c) plot the orbital-resolved band structures for the two spin-up bands in Fig. 6(a), where the royal blue dots in Fig. 6(b) and the violet dots in Fig. 6(c) denote the contributions from S p_z and S p_x/p_y orbitals to the bands, respectively. The sizes of the dots are proportional to the contribution of the corresponding orbitals. More interestingly, the bands around the Dirac energy degenerate K/K′ points in the two spin-up bands are mainly contributed by S p_z orbital, while the bands around the non-Dirac energy degenerate Γ point in the two spin-up bands are mainly contributed by S p_x/p_y orbitals, as clearly illustrated in Figs. 6(b) and 6(c). This kind of band structure possesses interesting topological properties, which will be discussed in the following section.

Figures 5(c) and 5(d) plot the spin-polarized band structures of the 6.0% compressive strained monolayer $NiAl_2S_4$ with the carrier doping concentration of 0.6 holes per unit cell and the 6.0% tensile-strained monolayer $NiAl_2S_4$ with the carrier doping concentration of 1.0 holes per unit cell. The band structures in Figs. 5(c) and 5(d) are still half-metallic states that exhibit 100% spin polarization with spin-up conducting channel around the E_F, indicating that the obtained high Curie temperature half-metallic states in hole-doped monolayer $NiAl_2S_4$ are robust against strain. By comparing the two spin-up bands around the E_F in Figs. 5(b)–5(d), we can observe that the slope of the quadratic non-Dirac bands around Γ point and the linear Dirac bands around K/K′ point can be tuned effectively by strain. The open direction of the highest spin-up quadratic non-Dirac band around Γ point is going downwards in Fig. 5(b), and its slope can be enlarged by applying compressive strain, as shown in Fig. 5(c), while its open direction can be tuned to upward by applying tensile strain, as illustrated in Fig. 5(d). Figure 6(d) shows that the magnified bands near the E_F of Fig. 5(d), from which we can observe that the quadratic non-Dirac energy degenerate Γ point and linear Dirac energy degenerate K/K′ point are all close to the E_F. Figures 6(e) and 6(f) plot the orbital-resolved band structures for the two spin-up bands in Fig. 6(d), showing that the bands around the Dirac energy degenerate K/K′ points and the bands around the non-Dirac energy degenerate Γ point in the two spin-up bands are mainly contributed by S p_z and S p_x/p_y orbitals, respectively, which is the same as the situation in the hole-doped monolayer $NiAl_2S_4$ without strain, as shown in Figs. 6(b) and 6(c).

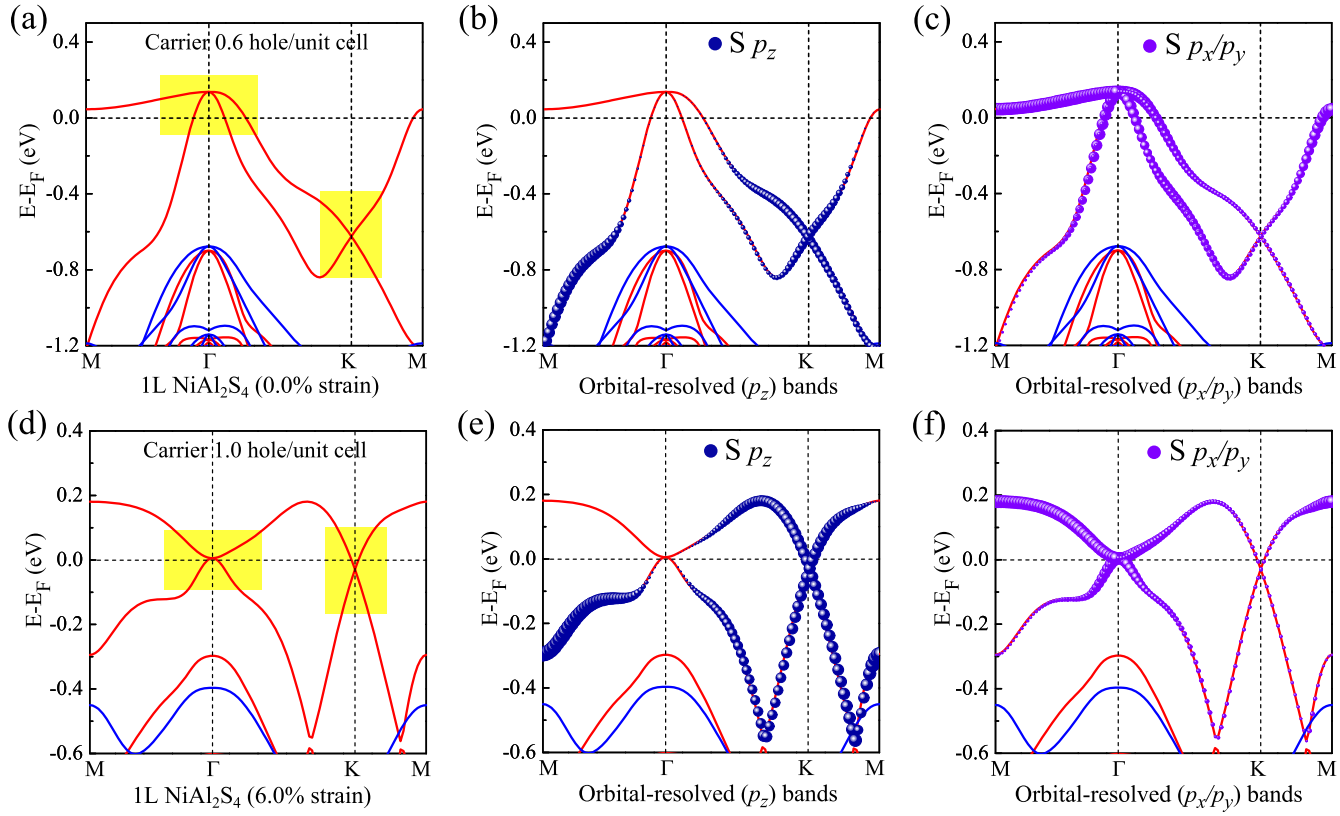

FIG. 6. (a) Spin-polarized band structure around the E_F for monolayer $NiAl_2S_4$ with the carrier doping concentration of 0.6 holes per unit cell. The red and blue curves denote the spin-up and spin-down bands, respectively. (b), (c) Orbital-resolved band structures of (a), where the contributions from S p_z and S p_x/p_y states to the bands are denoted by royal blue (b) and violet (c) dots. The sizes of the dots are proportional to the contribution of the corresponding orbitals. (d)–(f) Same as (a)–(c), except that the material system is 6.0% tensile-strained monolayer $NiAl_2S_4$ with the carrier doping concentration of 1.0 holes per unit cell.

D. High Chern number quantum anomalous Hall effect and topological mechanism

In previous studies, before considering SOC, the quadratic non-Dirac degenerate Γ point [42,62,63] and linear Dirac degenerate K/K′ points [14–17,33] have been widely reported to happen only separately in different 2D material systems. After the SOC is included, the degeneracy of the quadratic non-Dirac bands at the Γ point and linear Dirac bands at the K/K′ points will be eliminated and band gaps will be opened around the non-Dirac degenerate Γ point and Dirac degenerate K/K′ points. The theoretical works demonstrate that the SOC-induced local band gaps around the quadratic non-Dirac degenerate Γ point [42,62,63] and the linear Dirac degenerate K/K′ points [14–17,33] are both topologically nontrivial states, which can both produce the QSH effect (with time-reversal symmetry) and QAH effect (without time-reversal symmetry). For the fully spin-polarized quadratic non-Dirac bands, the SOC-induced band gap around the non-Dirac degenerate Γ point will be the QAH state with Chern number $C_{\mathrm{non-Dirac},\uparrow/\downarrow} = C_{\Gamma,\uparrow/\downarrow} = 1$ or -1 [42–44]. For the fully spin-polarized linear Dirac bands, the SOC-induced band gap around the Dirac degenerate K/K′ points will be the QAH state with Chern number $C_{\mathrm{Dirac},\uparrow/\downarrow} = C_{\mathrm{K},\uparrow/\downarrow} + C_{\mathrm{K}',\uparrow/\downarrow} = 1$ or -1 [33, 43, 44]. If the fully spin-polarized non-Dirac degenerate Γ point and Dirac degenerate K/K′ points simultaneously exist before SOC is included, the topologically trivial state with $C = 0$ (due to the Chern numbers around the non-Dirac Γ point and Dirac K/K′ points are the opposite signs, leading to the destructive coupling effect [43]) or high Chern number QAH state with $C = \pm 2$ (due to the Chern numbers around the non-Dirac Γ point and Dirac K/K′ points are the same signs, leading to the constructive coupling effect [45]) could be obtained when the SOC is considered.

Figure 7 plots the schematic depictions of the evolution of energy bands and topological properties of the fully spin-polarized non-Dirac bands, contributed by the multiple p_x/p_y orbitals, and the fully spin-polarized Dirac bands, contributed by the p_z orbital. Before including the SOC, the energy degenerate Γ point could be found respectively in the spin-up non-Dirac bands in Fig. 7(a) and the spin-down non-Dirac bands in Fig. 7(c). When the SOC is included, the band gap will be opened around the non-Dirac degenerate Γ point, as illustrated in Figs. 7(b) and 7(d). The obtained Berry curvatures $\Omega(\mathbf{k})$ around the Γ point when the E_F is located inside the SOC-induced energy gap in the spin-up non-Dirac bands are positive and with an approximate M shape, and the obtained Chern number is $C_\uparrow = 1$, as shown in Fig. 7(c), while for the spin-down non-Dirac bands, the obtained $\Omega(\mathbf{k})$ around the Γ point are negative and with an approximate W shape, and the obtained Chern number is $C_\downarrow = -1$, as shown in Fig. 7(d). Figures 7(e) and 7(g) show the spin-up and spin-down Dirac bands with energy degenerate K/K′ points. When the SOC

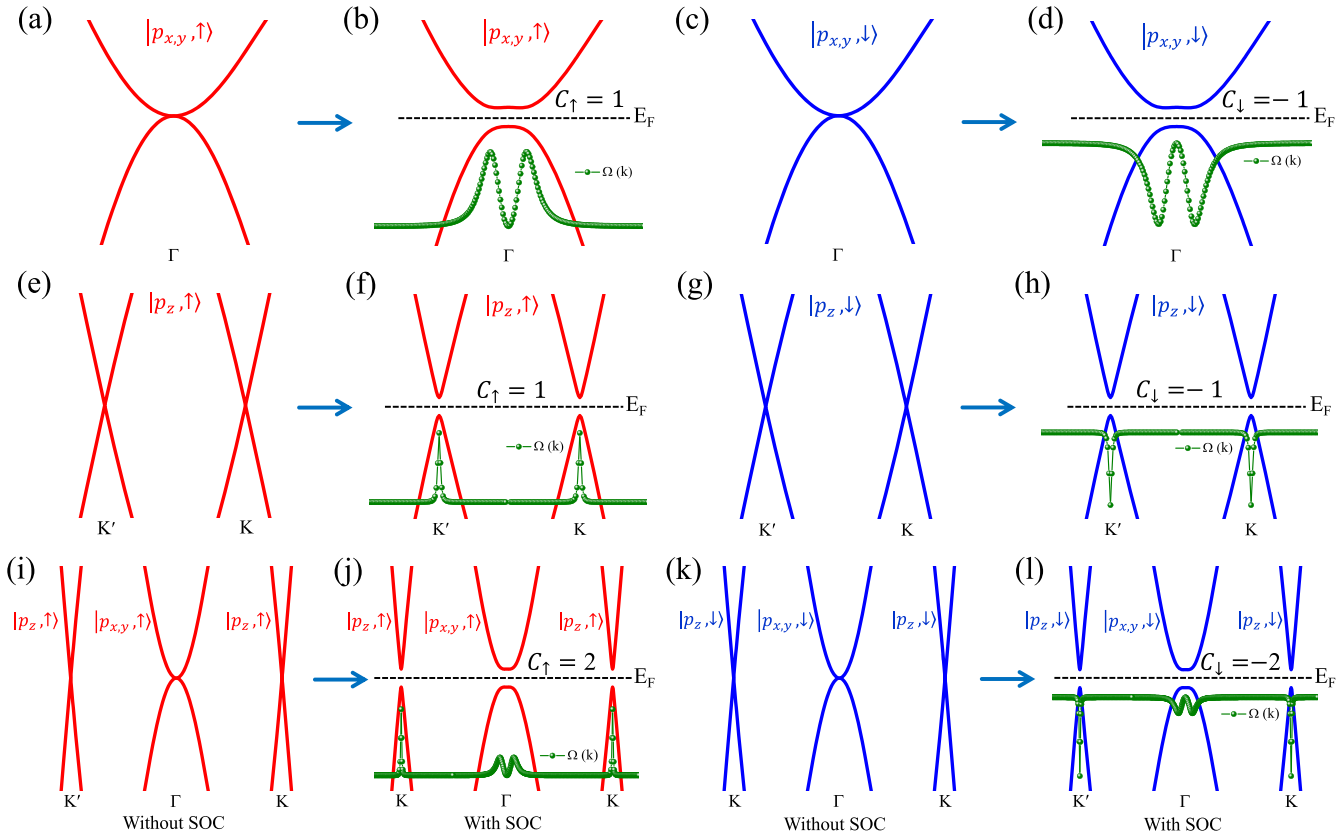

FIG. 7. (a)–(d) Schematic depictions of the evolution of energy bands and topological properties of the fully spin-polarized spin-up and spin-down non-Dirac bands. (a) The spin-up non-Dirac band structure without SOC formed by the p_x/p_y states. (b) The corresponding band structure of (a) by including SOC. The black dashed lines denote the E_F. (c), (d) Same as (a) and (b), except that the non-Dirac band is formed by the spin-down p_x/p_y states. (e)–(h) Schematic depictions of the evolution of energy bands and topological properties of the fully spin-polarized spin-up and spin-down Dirac bands. (e) The spin-up Dirac bands without SOC formed by the p_z state. (f) The corresponding band structure of (e) by including SOC. (g), (h) Same as (e) and (f), except that the Dirac band is formed by the spin-down p_z state. (i) The spin-up non-SOC band structure with non-Dirac bands at the Γ point formed by the p_x/p_y states and Dirac bands at the K/K′ points formed by the p_z state. (j) The corresponding band structure of (i) by including SOC. (k), (l) Same as (i) and (j), except that the non-Dirac bands and Dirac bands are formed by the spin-down p_x/p_y states and p_z state, respectively. The olive dots show the obtained Berry curvatures $\Omega(\mathbf{k})$ when the E_F is located inside the SOC-induced energy gap.

is considered, the band gap will be opened at the Dirac K/K′ points. If the E_F is located inside the SOC-induced energy gap, the Chern number of $C_\uparrow = 1$ for the spin-up Dirac bands and $C_\downarrow = -1$ for the spin-down Dirac bands will be obtained, as illustrated in Figs. 7(f) and 7(h). Figures 7(i) and 7(k) show the spin-up and spin-down bands with non-Dirac degenerate Γ point and Dirac degenerate K/K′ points simultaneously exist. When the SOC is considered, the band gap will be opened at the non-Dirac Γ and Dirac K/K′ points. If the E_F is located inside the SOC-induced global band gap, the Chern number of $C_\uparrow = C_{\text{non-Dirac},\uparrow} + C_{\text{Dirac},\uparrow} = 2$ for the spin-up bands and $C_\downarrow = C_{\text{non-Dirac},\downarrow} + C_{\text{Dirac},\downarrow} = -2$ for the spin-down bands will be obtained, indicating the realization of a high Chern number QAH effect, as illustrated in Figs. 7(j) and 7(l).

Figure 8(a) shows the magnified bands around the E_F for the 6.0% tensile-strained monolayer $NiAl_2S_4$ with the carrier doping concentration of 1.0 holes per unit cell, in which the non-Dirac degenerate Γ point is above the E_F and the Dirac degenerate K/K′ points is below the E_F. The red curves denote the spin-up bands without SOC. The orbital-resolved band structures in Fig. 6 show that the non-Dirac bands around the Γ point and Dirac bands around the K/K′ points are dominated by S p_x/p_y orbitals and S p_z orbital, respectively, the same as the schematic spin-up bands in Fig. 7(i). Figure 8(b) displays the corresponding band structure of Fig. 8(a) with the consideration of SOC, from which we can observe that the SOC-induced local band gap of Δ_Γ (10.3 meV) around the non-Dirac Γ point and local band gap of Δ_K (11.2 meV) around the Dirac K/K′ points are clearly illustrated. The Berry curvatures $\Omega(\mathbf{k})$ and Chern numbers are calculated to identify the topological properties of the SOC-induced band gap. The Berry curvatures are calculated by [64,65]

$$\Omega(\mathbf{k}) = \sum_n f_n \Omega_n(\mathbf{k}), \tag{3}$$

$$\Omega_n(\mathbf{k}) = -2\text{Im}\sum_{m\neq n} \frac{\hbar^2 \langle \psi_{n\mathbf{k}} | v_x | \psi_{m\mathbf{k}} \rangle \langle \psi_{m\mathbf{k}} | v_y | \psi_{n\mathbf{k}} \rangle}{(E_m - E_n)^2}, \tag{4}$$

where f_n is the Fermi-Dirac distribution function, $v_{x(y)}$ are the velocity operators, E_n is the eigenvalue of the Bloch functions $|\psi_{n\mathbf{k}}\rangle$, and the summation is over all the occupied states. The Chern number C can be obtained by integrating

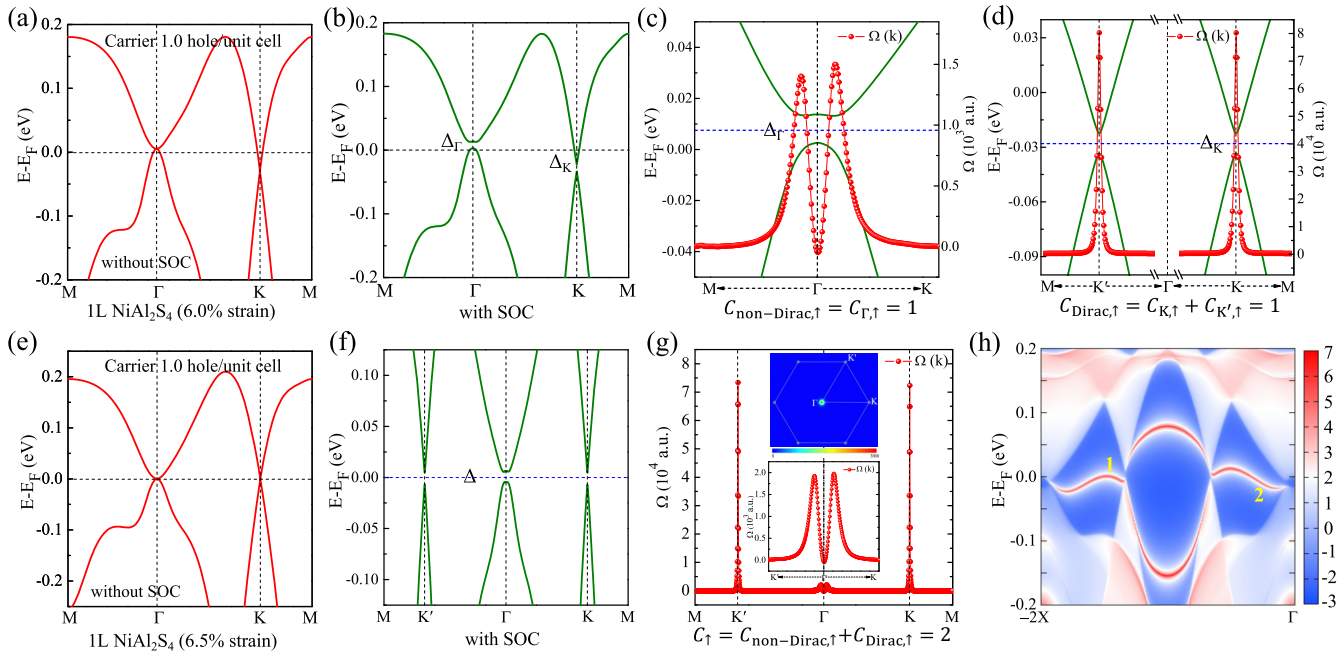

FIG. 8. (a) The magnified bands of Fig. 6(d) around the E_F. The red curves denote the spin-up bands. (b) The corresponding band structure of (a) with the consideration of SOC. (c) The magnified bands of (b) around the SOC-induced gap Δ_Γ. The red dots in (c) show the calculated Berry curvatures $\Omega(\mathbf{k})$ when the E_F is set to be located inside the gap Δ_Γ. (d) The magnified bands of (b) around the SOC-induced gap Δ_K at K/K′ points. The red dots in (d) show the calculated $\Omega(\mathbf{k})$ when the E_F is set to be located inside the gap Δ_K. (e) Spin-polarized band structure around the E_F for 6.5% tensile-strained monolayer $NiAl_2S_4$ with a carrier doping concentration of 1.0 holes per unit cell. (f) The corresponding band structure of (e) with the consideration of SOC. (g) The obtained $\Omega(\mathbf{k})$ when the E_F is located inside the global band gap shown in (f). The bottom inset shows the magnified $\Omega(\mathbf{k})$ around Γ point. The top inset shows the 2D distribution of the $\Omega(\mathbf{k})$ in the momentum space. (h) The calculated density of states of the semi-infinite 6.5% tensile-strained monolayer $NiAl_2S_4$ with the carrier doping concentration of 1.0 holes per unit cell.

the Berry curvatures over the first Brillouin Zone, as $C = \frac{1}{2\pi}\sum_n \int_{BZ} d^2k\Omega_n$. The olive curves in Fig. 8(c) show the magnified band of Fig. 8(b) around the SOC-induced band gap Δ_Γ. The red dots in Fig. 8(c) display the calculated $\Omega(\mathbf{k})$ around the non-Dirac Γ point when the E_F is located inside Δ_Γ. We can observe that the large values of the obtained $\Omega(\mathbf{k})$ mainly distribute around Δ_Γ with an approximate M shape, which is the same as the $\Omega(\mathbf{k})$ plotted for the spin-up non-Dirac bands in Fig. 7(b). By integrating the obtained $\Omega(\mathbf{k})$ around the non-Dirac Γ point, the nonzero integer Chern number of $C_{non-Dirac,\uparrow} = C_{\Gamma,\uparrow} = 1$ is obtained, indicating the SOC-induced local non-Dirac energy gap Δ_Γ is the topologically nontrivial state with $C_\uparrow = 1$. The olive curves in Fig. 8(d) show the magnified band of Fig. 8(b) around the SOC-induced band gap Δ_K. The red dots in Fig. 8(d) illustrate the calculated $\Omega(\mathbf{k})$ around the Dirac K and K′ points when the E_F is located inside Δ_K, from which we can find that large values of the obtained $\Omega(\mathbf{k})$ mainly distribute around the Dirac K and K′ points. By integrating the obtained $\Omega(\mathbf{k})$ around the Dirac K and K′ points, the nonzero integer Chern number of $C_{Dirac,\uparrow} = C_{K,\uparrow} + C_{K',\uparrow} = 1$ is obtained, indicating the SOC induced local Dirac energy gap at K/K′ points is the topologically nontrivial state with $C_\uparrow = 1$.

The band structures of the 6.5% tensile-strained monolayer $NiAl_2S_4$ with the variation of hole doping concentrations are given in Fig. S17 in Supplemental Material [57]. Figure 8(e) shows the spin-polarized band structure around the E_F for 6.5% tensile-strained monolayer $NiAl_2S_4$ with the carrier doping concentration of 1.0 holes per unit cell, from which we can observe that the non-Dirac degenerate Γ point and the Dirac degenerate K/K′ points are all located at the E_F. When the SOC is included, a global band gap $\Delta = 9.2$ meV is opened, as shown in Fig. 8(f). Figure 8(g) displays the calculated $\Omega(\mathbf{k})$ along the high-symmetry lines, including non-Dirac Γ point and Dirac K and K′ points. The obtained $\Omega(\mathbf{k})$ around the K and K′ points have the same signs, and both are in peak shapes with positive values. In addition, the $\Omega(\mathbf{k})$ around the Γ point mainly are positive values and in the M shape, as clearly illustrated in Fig. 8(g). The distribution of $\Omega(\mathbf{k})$ in Fig. 8(g) is the same as the $\Omega(\mathbf{k})$ plotted for the spin-up bands with the coexistence of non-Dirac Γ point and Dirac K/K′ points in Fig. 7(j). The top inset in Fig. 8(g) displays the distribution of $\Omega(\mathbf{k})$ in 2D momentum space, showing that the $\Omega(\mathbf{k})$ around the non-Dirac Γ point and Dirac K/K′ points are with the same signs. By integrating the obtained $\Omega(\mathbf{k})$ over the first BZ, the nonzero integer Chern number of $C_\uparrow = C_{non-Dirac,\uparrow} + C_{Dirac,\uparrow} = 2$ is obtained, indicating the SOC-induced global band gap Δ in Fig. 8(f) is a high Chern number QAH state with $C = 2$. Figure 8(h) plots the calculated DOS of the semi-infinite system, from which we can observe that two topologically nontrivial edge states connecting the conduction and valence bands exist inside the SOC-induced gap Δ, confirming the obtained high Chern number of $C = 2$. Therefore, we predict a realistic 2D

magnetic material system that can produce the high Chern number QAH effect through the constructive coupling effect [45] between the topological nontrivial non-Dirac and Dirac states. The phase diagram of the global band gap (topological phase) is given in Fig. S18 in the Supplemental Material [57], showing that the global band gap (QAH state with $C = 2$) can be obtained in the 6.2% to 6.8% tensile-strained monolayer $NiAl_2S_4$ with the carrier doping concentration of 1.0 holes per unit cell.

To deeply understand the formation mechanism of the special band structure [Fig. 8(e)] with non-Dirac and Dirac states in monolayer $NiAl_2S_4$, an effective tight-binding (TB) model Hamiltonian is constructed. Since the non-Dirac and Dirac states in Fig. 8(e) are dominated by the p_x, p_y, and p_z states of the S atoms, it is reasonable to adopt the p_x, p_y, and p_z orbitals of the S atoms as the basis. To simplify the TB model and the calculations, we consider the two S atom layers in the middle of the atomic crystal structure to construct the effective TB model. The simplified lattice can be denoted as the 2D buckled honeycomb lattice, in which the A and B sublattices are not coplanar. The total effective TB model Hamiltonian of this 2D buckled honeycomb lattice in the basis of (p_{Ax}, p_{Ay}, p_{Az}, p_{Bx}, p_{By}, p_{Bz}) can be written as

$$\begin{aligned} H(k) &= H_{\text{hop}}(k) + H_{\text{SOC}} - H_M \\ &= \begin{bmatrix} H_{\text{hop}\uparrow\uparrow} & 0 \\ 0 & H_{\text{hop}\downarrow\downarrow} \end{bmatrix} + \begin{bmatrix} H_{\text{SOC}\uparrow\uparrow} & H_{\text{SOC}\uparrow\downarrow} \\ H_{\text{SOC}\downarrow\uparrow} & H_{\text{SOC}\downarrow\downarrow} \end{bmatrix} \\ &\quad - \begin{bmatrix} M\mathbf{I} & 0 \\ 0 & M\mathbf{I} \end{bmatrix}, \end{aligned} \tag{5}$$

where H_{hop}, H_{SOC}, and H_M represent the NN hopping term, the on-site SOC term, and the magnetic exchange field term, respectively. The up and down arrows denote the spin-up and spin-down channels, respectively. M is the exchange field strength, and $\mathbf{I}$ in Eq. (5) is a unit matrix.

The hopping terms for the spin-up and spin-down channels can be expressed as

$$H_{\text{hop}\uparrow\uparrow} = H_{\text{hop}\downarrow\downarrow} = \begin{bmatrix} H^{AA} & H^{AB} \\ H^{BA} & H^{BB} \end{bmatrix}, \tag{6}$$

where the diagonal matrix elements are the on-site energies for the three orbitals, and A and B refer to the nonequivalent A and B sites in the unit cell. The H^{AA} and H^{BB} can be written as

$$H^{AA} = H^{BB} = \begin{bmatrix} \varepsilon_{p_x} & 0 & 0 \\ 0 & \varepsilon_{p_y} & 0 \\ 0 & 0 & \varepsilon_{p_z} \end{bmatrix}, \tag{7}$$

where ε_{p_x}, ε_{p_y}, and ε_{p_z} are the on-site energies for the p_x, p_y, and p_z orbitals, respectively. The off-diagonal block matrices include the hopping interactions between the A and B sites. The H^{AB} and H^{BA} can be written as

$$H^{AB} = \begin{bmatrix} h^{AB}_{xx} & h^{AB}_{xy} & h^{AB}_{xz} \\ h^{AB}_{yx} & h^{AB}_{yy} & h^{AB}_{yz} \\ h^{AB}_{zx} & h^{AB}_{zy} & h^{AB}_{zz} \end{bmatrix}, H^{BA} = (H^{AB})^*, \tag{8}$$

in which

$$\begin{aligned} h^{AB}_{xx} &= \frac{1}{1+d^2} e^{ik_x}(V_{pp\sigma} + d^2 V_{pp\pi}) + \frac{1}{1+d^2} e^{i\left(-\frac{1}{2}k_x\right)} \\ &\quad \times \cos\left(\frac{\sqrt{3}}{2}k_y\right)\left[\frac{1}{2}V_{pp\sigma} + \left(\frac{3}{2} + 2d^2\right)V_{pp\pi}\right], \\ h^{AB}_{xy} &= \frac{\sqrt{3}i}{2(1+d^2)} e^{i\left(-\frac{1}{2}k_x\right)} \sin\left(\frac{\sqrt{3}}{2}k_y\right)(V_{pp\pi} - V_{pp\sigma}), \\ h^{AB}_{xz} &= \frac{d}{1+d^2}\left[e^{i\left(-\frac{1}{2}k_x\right)} \cos\left(\frac{\sqrt{3}}{2}k_y\right) - e^{ik_x}\right](V_{pp\pi} - V_{pp\sigma}), \\ h^{AB}_{yy} &= e^{ik_x} V_{pp\pi} + \frac{1}{1+d^2} e^{i\left(-\frac{1}{2}k_x\right)} \\ &\quad \times \cos\left(\frac{\sqrt{3}}{2}k_y\right)\left[\frac{3}{2}V_{pp\sigma} + \left(\frac{1}{2} + 2d^2\right)V_{pp\pi}\right], \\ h^{AB}_{yz} &= \frac{-\sqrt{3}di}{1+d^2} e^{i\left(-\frac{1}{2}k_x\right)} \sin\left(\frac{\sqrt{3}}{2}k_y\right)(V_{pp\pi} - V_{pp\sigma}), \\ h^{AB}_{zz} &= e^{ik_x}\left[\frac{d^2}{1+d^2}V_{pp\sigma} + \frac{1}{1+d^2}V_{pp\pi}\right] \\ &\quad + 2e^{i\left(-\frac{1}{2}k_x\right)} \cos\left(\frac{\sqrt{3}}{2}k_y\right)\left[\frac{d^2}{1+d^2}V_{pp\sigma} + \frac{1}{1+d^2}V_{pp\pi}\right], \\ h^{AB}_{yx} &= h^{AB}_{xy}, h^{AB}_{zx} = h^{AB}_{xz}, h^{AB}_{zy} = h^{AB}_{yz}, \end{aligned} \tag{9}$$

where $V_{pp\sigma}$ and $V_{pp\pi}$ are the NN hopping parameters corresponding to the σ and π bonds formed by p_x, p_y, and p_z orbitals. The d parameter denotes the effective height difference between the nonequivalent A and B sublattices.

The on-site SOC terms can be written as

$$H_{\text{SOC}} = \begin{bmatrix} H_{\text{SOC}\uparrow\uparrow} & H_{\text{SOC}\uparrow\downarrow} \\ H_{\text{SOC}\downarrow\uparrow} & H_{\text{SOC}\downarrow\downarrow} \end{bmatrix}, \tag{10}$$

in which

$$\begin{aligned} H_{\text{SOC}\uparrow\uparrow/\downarrow\downarrow} &= s \cdot \lambda \begin{bmatrix} H^c_{\text{SOC}} & 0 \\ 0 & H^c_{\text{SOC}} \end{bmatrix}, \\ H_{\text{SOC}\uparrow\downarrow/\downarrow\uparrow} &= w \cdot \lambda \begin{bmatrix} H^u_{\text{SOC}} & 0 \\ 0 & H^u_{\text{SOC}} \end{bmatrix}, \\ H^c_{\text{SOC}} &= \begin{bmatrix} 0 & -i & 0 \\ i & 0 & 0 \\ 0 & 0 & 0 \end{bmatrix}, H^u_{\text{SOC}} = \begin{bmatrix} 0 & 0 & 1 \\ 0 & 0 & -wi \\ -1 & wi & 0 \end{bmatrix}, \end{aligned} \tag{11}$$

where λ is the atomic SOC strength, $s = +1$ for $H_{\text{SOC}\uparrow\uparrow}$, $s = -1$ for $H_{\text{SOC}\downarrow\downarrow}$, $w = +1$ for $H_{\text{SOC}\uparrow\downarrow}$, and $w = -1$ for $H_{\text{SOC}\downarrow\uparrow}$.

The calculated band structures of the above-constructed effective TB model Hamiltonian are given in Fig. 9. The TB parameters adopted in Fig. 9(a) are $d = 0.23$, $\varepsilon_{p_x} = \varepsilon_{p_y} = -0.47\,\text{eV}$, $\varepsilon_{p_z} = -0.27\,\text{eV}$, $V_{pp\sigma} = 0.56\,\text{eV}$, $V_{pp\pi} = -0.21\,\text{eV}$, $M = 0.0\,\text{eV}$, and $\lambda = 0.0\,\text{eV}$, where only the hopping term is considered. Figure 9(b) shows the magnified bands in the red dashed rectangle box in Fig. 9(a), from which we can observe that the bands around $E = 0.0\,\text{eV}$ are not only degenerate at the Γ point with quadratic non-Dirac band dispersion but also degenerate at the K point with linear Dirac

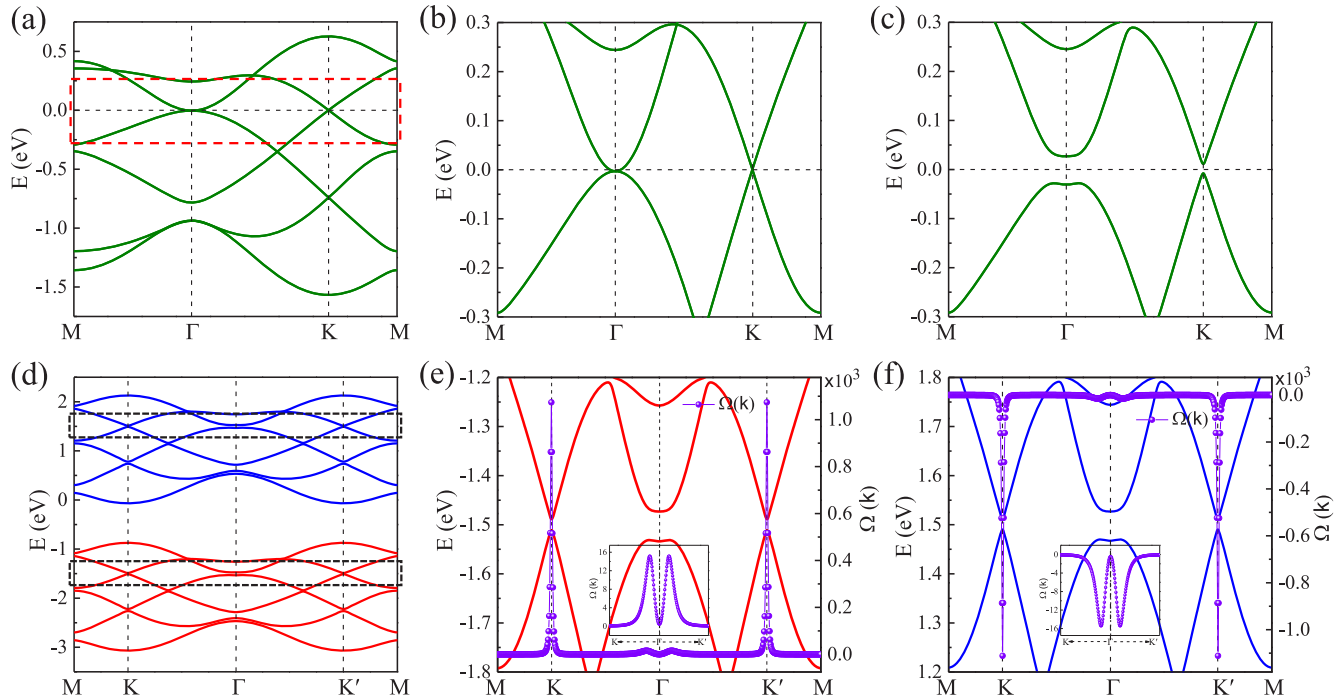

FIG. 9. (a) The band structure calculated from the effective TB model with three orbitals (p_x, p_y, p_z) per nonequivalent lattice site. The parameters adopted are $d = 0.23$, $\varepsilon_{p_x} = \varepsilon_{p_y} = -0.47$ eV, $\varepsilon_{p_z} = -0.27$ eV, $V_{pp\sigma} = 0.56$ eV, $V_{pp\pi} = -0.21$ eV, $M = 0.0$ eV, and $\lambda = 0.0$ eV. (b) The magnified bands in the red dashed rectangle box in (a). (c) The corresponding band structure of (b) by including the SOC ($\lambda = 0.03$ eV). (d) The TB band structure with the parameters adopted in (a), except that the magnetic exchange field and SOC are included by setting $M = 1.5$ eV and $\lambda = 0.03$ eV. The red and blue curves denote the spin-up and spin-down bands, respectively. (e) The magnified spin-up bands in the black dashed rectangle box in (d) around $E = -1.5$ eV. (f) The magnified spin-down bands in the black dashed rectangle box in (d) around $E = 1.5$ eV. The violet dots in (e) and (f) show the calculated Berry curvatures when the E_F is set within the SOC-induced band gap. The insets in (e) and (f) show the magnified Berry curvatures around the Γ point.

band dispersion. When SOC is considered, the degeneracies at the Γ and K point are both eliminated, and band gaps are opened around these points, as illustrated in Fig. 9(c) with $\lambda = 0.03$ eV. Figure 9(d) plots the corresponding band structure of Fig. 9(a) by further considering the magnetic exchange field (with $M = 1.5$ eV) and SOC ($\lambda = 0.03$ eV), in which the spin-up (red curves) and spin-down (blue curves) bands are fully spin polarized. Figure 9(e) shows the magnified spin-up bands around $E = -1.5$ eV in Fig. 9(d), whose bands characteristic are the same as that in Fig. 8(f). The distributions of the calculated $\Omega(k)$ in Fig. 9(e) are the same as the DFT results displayed in Fig. 8(g). By integrating the obtained $\Omega(k)$, we obtain $C_{(\text{non-Dirac},\uparrow)} = C_{(\Gamma,\uparrow)} = 1$ and $C_{(\text{Dirac},\uparrow)} = C_{(K,\uparrow)} + C_{(K',\uparrow)} = 1$, the total Chern number is $C_\uparrow = C_{(\text{non-Dirac},\uparrow)} + C_{(\text{Dirac},\uparrow)} = 2$, indicating the SOC induced global band gap in Fig. 9(e) is a high Chern number QAH state with $C = 2$. For the spin-down bands in Fig. 9(f), the Chern numbers of $C_{(\text{non-Dirac},\downarrow)} = -1$, $C_{(\text{Dirac},\downarrow)} = C_{(K,\downarrow)} + C_{(K',\downarrow)} = -1$, and $C_\downarrow = C_{(\text{non-Dirac},\downarrow)} + C_{(\text{Dirac},\downarrow)} = -2$ can be obtained, indicating the SOC-induced global band gap in Fig. 9(f) is a high Chern number QAH state with $C = -2$. The calculated TB band structures, Berry curvatures, and Chern numbers indicate that the obtained interesting band structure [Figs. 8(e) and 8(f)] with the coexistence of non-Dirac and Dirac states and the high Chern number QAH effect in monolayer $NiAl_2S_4$ can be described well though the constructed effective TB model.

Not only are the monolayer $NiAl_2S_4$ are systematically investigated, the structural, magnetic configurations, electronic band structures, strain effect, and carrier doping effect of the monolayer TM-Al_2S_4 (TM=Mn, Fe, Cr, V) are also investigated. The calculated results are given in the Supporting Note 1 in Supplemental Material [57]. In addition, the structural, magnetic configurations, and electronic band structures of the bulk TM-Al_2S_4 (TM = Mn, Fe, Cr, V, Ni) are also studied. The obtained results are given in the Supporting Note 1 and Note 2 in Supplemental Material [57].

IV. CONCLUSIONS

In summary, the electronic structures, magnetic properties, and topological properties of the monolayer $NiAl_2S_4$ are systematically investigated by using first-principles calculations. The calculation results of the formation energy, phonon spectrum, and AIMD simulations demonstrate that the monolayer $NiAl_2S_4$ is dynamically and thermally stable. Three typical magnetic configurations of FM, collinear AFM, and noncollinear 120^0-AFM for the 2D triangular lattice are considered to explore the magnetic properties of the intrinsic, stained, and carrier-doped monolayer $NiAl_2S_4$. The monolayer $NiAl_2S_4$ is in the 120^0-AFM state and is a semiconductor with an indirect band gap of 1.52 eV. In addition, its magnetic properties can be tuned effectively by carrier doping.

The FM state can be achieved in monolayer $NiAl_2S_4$ and the T_C increases rapidly with the increase of hole-doping concentration. Remarkably, the hole-doped monolayer $NiAl_2S_4$ in FM states are half metals, and the room-temperature FM half-metallic state can be realized. The FM half-metallic state obtained in the hole-doped monolayer $NiAl_2S_4$ is robust against strain. For the hole-doped monolayer $NiAl_2S_4$ in the half-metallic state, before the SOC is included, the two spin-up bands around the E_F are not only degenerate at the Γ point with quadratic non-Dirac band dispersions but also degenerates at the K/K′ points with linear Dirac band dispersions. The non-Dirac bands at the Γ point and Dirac bands at K/K′ points are mainly contributed by S p_x/p_y orbitals and S p_z orbital, respectively. After the SOC is considered, the local topologically nontrivial band gaps with Chern number $C = 1$ will be opened, respectively, around the non-Dirac degenerate Γ point and Dirac degenerate K/K′ points. The high Chern number QAH effect with $C = 2$ can be achieved in the 6.2% to 6.8% tensile-strained monolayer $NiAl_2S_4$ with the carrier doping concentration of 1.0 holes per unit cell, through the constructive coupling effect between the topologically nontrivial non-Dirac and Dirac states. Our findings demonstrate that monolayer $NiAl_2S_4$ possesses rich physical properties and is promising for the experimental exploration of high T_C spintronic devices and high Chern number QAH effect.

ACKNOWLEDGMENTS

This work was supported by the National Natural Science Foundation of China (Grants No. 11904250 and No. 11747137) and the Qing Lan Project of Jiangsu Province.

[1] C. L. Kane and E. J. Mele, Quantum Spin Hall Effect in Graphene, Phys. Rev. Lett. **95**, 226801 (2005).

[2] F. Reis, G. Li, L. Dudy, M. Bauernfeind, S. Glass, W. Hanke, R. Thomale, J. Schäfer, and R. Claessen, Bismuthene on a SiC substrate: A candidate for a high-temperature quantum spin Hall material, Science **357**, 287 (2017).

[3] G. B. Liu, D. Xiao, Y. G. Yao, X. D. Xu, and W. Yao, Electronic structures and theoretical modelling of two-dimensional group-VIB transition metal dichalcogenides, Chem. Soc. Rev. **44**, 2643 (2015).

[4] A. K. Geim and K. S. Novoselov, The rise of graphene, Nat. Mater. **6**, 183 (2007).

[5] C. R. Dean, A. F. Young, I. Meric1, C. Lee, L. Wang, S. Sorgenfrei, K. Watanabe, T. Taniguchi, P. Kim, K. L. Shepard, and J. Hone, Boron nitride substrates for high-quality graphene electronics, Nat. Nanotechnol. **5**, 722 (2010).

[6] Q. H. Wang, K. Kalantar-Zadeh, A. Kis, J. N. Coleman, and M. S. Strano, Electronics and optoelectronics of two-dimensional transition metal dichalcogenides, Nat. Nanotechnol. **7**, 699 (2012).

[7] R. A. de Groot, F. M. Mueller, P. G. van Engen, and K. H. J. Buschow, Phys. Rev. Lett. **50**, 2024 (1983).

[8] X. X. Li, X. J. Wu, Z. Y. Li, J. L. Yang, and J. G. Hou, Bipolar magnetic semiconductors: A new class of spintronics materials, Nanoscale **4**, 5680 (2012).

[9] X. X. Li and J. L. Yang, First-principles design of spintronics materials, Natl. Sci. Rev. **3**, 365 (2016).

[10] X. X. Li and J. L. Yang, CrXTe$_3$ (X = Si, Ge) nanosheets: Two dimensional intrinsic ferromagnetic semiconductors, J. Mater. Chem. C **2**, 7071 (2014).

[11] N. Sivadas, M. W. Daniels, R. H. Swendsen, S. Okamoto, and D. Xiao, Magnetic ground state of semiconducting transition-metal trichalcogenide monolayers, Phys. Rev. B **91**, 235425 (2015).

[12] W. B. Zhang, Q. Qu, P. Zhu, and C. H. Lam, Robust intrinsic ferromagnetism and half semiconductivity in stable two-dimensional single-layer chromium trihalides, J. Mater. Chem. C **3**, 12457 (2015).

[13] X. L. Sheng and B. K. Nikolic, Monolayer of the 5d transition metal trichloride $OsCl_3$: A playground for two-dimensional magnetism, room-temperature quantum anomalous Hall effect, and topological phase transitions, Phys. Rev. B **95**, 201402(R) (2017).

[14] J. He, X. Li, P. Lyu, and P. Nachtigall, Near-room-temperature Chern insulator and Dirac spin-gapless semiconductor: Nickel chloride monolayer, Nanoscale **9**, 2246 (2017).

[15] C. Huang, J. Zhou, H. Wu, K. Deng, P. Jena, and E. J. Kan, Quantum anomalous Hall effect in ferromagnetic transition metal halides, Phys. Rev. B **95**, 045113 (2017).

[16] Q. Sun and N. Kioussis, Prediction of manganese trihalides as two-dimensional Dirac half-metals, Phys. Rev. B **97**, 094408 (2018).

[17] J. He, S. Ma, P. Lyu, and P. Nachtigall, Unusual Dirac half-metallicity with intrinsic ferromagnetism in vanadium trihalide monolayers, J. Mater. Chem. C **4**, 2518 (2016).

[18] B. Huang, G. Clark, E. Navarro-Moratalla, D. R. Klein, R. Cheng, K. L. Seyler, D. Zhong, E. Schmidgall, M. A. McGuire, D. H. Cobden, W. Yao, D. Xiao, P. Jarillo-Herrero, and X. D. Xu, Layer-dependent ferromagnetism in a van der Waals crystal down to the monolayer limit, Nature (London) **546**, 270 (2017).

[19] C. Gong, L. Li, Z. Li, H. Ji, A. Stern, Y. Xia, T. Cao, W. Bao, C. Wang, Y. Wang, Z. Q. Qiu, R. J. Cava, S. G. Louie, J. Xia, and X. Zhang, Discovery of intrinsic ferromagnetism in two-dimensional van der Waals crystals, Nature (London) **546**, 265 (2017).

[20] H. B. Wang, F. Fan, S. Zhu, and H. Wu, Doping enhanced ferromagnetism and induced half-metallicity in CrI_3 monolayer, Europhys. Lett. **114**, 47001 (2016).

[21] J. Y. Zhang, B. Zhao, C. L. Ma, and Z. Q. Yang, Bipolar ferromagnetic semiconductors and doping-tuned room-temperature half-metallicity in monolayer MoX_3 (X = Cl, Br, I): An HSE06 study, Phys. Rev. B **103**, 075433 (2021).

[22] X. X. Li, X. J. Wu, and J. L. Yang, Half-metallicity in MnPSe3 exfoliated nanosheet with carrier doping, J. Am. Chem. Soc. **136**, 11065 (2014).

[23] K. He, Y. Y. Wang, and Q. K. Xue, Quantum anomalous Hall effect, Natl. Sci. Rev. **1**, 38 (2014).

[24] X. L. Qi, and S. C. Zhang, Topological insulators and superconductors, Rev. Mod. Phys. **83**, 1057 (2011).

[25] F. D. M. Haldane, Model for a Quantum Hall Effect without Landau Levels: Condensed-Matter Realization of the Parity Anomaly, Phys. Rev. Lett. **61**, 2015 (1988).

[26] R. Yu, W. Zhang, H. J. Zhang, S. C. Zhang, X. Dai, and Z. Fang, Quantized anomalous Hall effect in magnetic topological insulators, Science **329**, 61 (2010).

[27] Z. H. Qiao, S. A. Yang, W. X. Feng, W. K. Tse, J. Ding, Y. G. Yao, J. Wang, and Q. Niu, Quantum Anomalous Hall Effect in Graphene from Rashba and Exchange Effects, Phys. Rev. B **82**, 161414(R) (2010).

[28] Z. H. Qiao, W. Ren, H. Chen, L. Bellaiche, Z. Y. Zhang, A. H. MacDonald, and Q. Niu, Quantum Anomalous Hall Effect in Graphene Proximity Coupled to an Antiferromagnetic Insulator, Phys. Rev. Lett. **112**, 116404 (2014).

[29] J. Y. Zhang, B. Zhao, Y. G. Yao, and Z. Q. Yang, Robust quantum anomalous Hall effect in graphene-based van der Waals heterostructures, Phys. Rev. B **92**, 165418 (2015).

[30] J. Y. Zhang, B. Zhao, T. Zhou, Y. Xue, C. L. Ma, and Z. Q. Yang, Strong magnetization and Chern insulators in compressed graphene/CrI_3 van der Waals heterostructures, Phys. Rev. B **97**, 085401 (2018).

[31] M. Ezawa, Valley-Polarized Metals and Quantum Anomalous Hall Effect in Silicene, Phys. Rev. Lett. **109**, 055502 (2012).

[32] J. H. Qian, J. Y. Zhang, Q. X. Wu, and Z. H. Lin, Robust Quantum Anomalous Hall Effect with Electrically Tunable Band Gap in Ta-Decorated Silicene, Appl. Phys. Lett. **114**, 053105 (2019).

[33] Z. F. Wang, Z. Liu, and F. Liu, Quantum Anomalous Hall Effect in 2D Organic Topological Insulators, Phys. Rev. Lett. **110**, 196801 (2013).

[34] Z. Liu, Z. F. Wang, J. W. Mei, Y. S. Wu, and F. Liu, Flat Chern Band in a Two-Dimensional Organometallic Framework, Phys. Rev. Lett. **110**, 106804 (2013).

[35] Z. Y. Li, Y. L. Han, and Z. H. Qiao, Chern Number Tunable Quantum Anomalous Hall Effect in Monolayer Transitional Metal Oxides Via Manipulating Magnetization Orientation, Phys. Rev. Lett. **129**, 036801 (2022).

[36] J. Li, Y. Li, S. Du, Z. Wang, B. L. Gu, S. C. Zhang, K. He, W. Duan, and Y. Xu, Intrinsic magnetic topological insulators in van der Waals layered $MnBi_2Te_4$-family materials, Sci. Adv. **5**, eaaw5685 (2019).

[37] D. Q. Zhang, M. J. Shi, T. S. Zhu, D. Y. Xing, H. J. Zhang, and J. Wang, Topological Axion States in the Magnetic Insulator $MnBi_2Te_4$ with the Quantized Magnetoelectric Effect, Phys. Rev. Lett. **122**, 206401 (2019).

[38] C. Z. Chang, J. S. Zhang, X. Feng, J. Shen, Z. C. Zhang, M. H. Guo, K. Li, Y. B. Ou, P. Wei, L. L. Wang, Z. Q. Ji, Y. Feng, S. H. Ji, X. Chen, J. F. Jia, X. Dai, Z. Fang, S. C. Zhang, K. He, Y. Y. Wang *et al.*, Experimental observation of the quantum anomalous Hall effect in a magnetic topological insulator, Science **340**, 167 (2013).

[39] X. F. Kou, S. T. Guo, Y. B. Fan, L. Pan, M. Lang, Y. Jiang, Q. M. Shao, T. X. Nie, K. Murata, J. S. Tang, Y. Wang, L. He, T. K. Lee, W. L. Lee, and K. L. Wang, Scale-Invariant Quantum Anomalous Hall Effect in Magnetic Topological Insulators Beyond the Two-Dimensional Limit, Phys. Rev. Lett. **113**, 137201 (2014).

[40] Y. J. Deng, Y. J. Yu, M. Z. Shi, Z. X. Guo, Z. H. Xu, J. Wang, X. H. Chen, and Y. B. Zhang, Quantum anomalous Hall effect in intrinsic magnetic topological insulator $MnBi_2Te_4$, Science **367**, 895 (2020).

[41] B. A. Bernevig, T. L. Hughes, and S. C. Zhang, Quantum spin Hall effect and topological phase transition in HgTe quantum wells, Science **314**, 1757 (2006).

[42] Q. F. Liang, R. Yu, J. Zhou, and X. Hu, Topological states of non-Dirac electrons on a triangular lattice, Phys. Rev. B **93**, 035135 (2016).

[43] J. Y. Zhang, B. Zhao, Y. Xue, T. Zhou, and Z. Q. Yang, Coupling effect of topological states and Chern insulators in two-dimensional triangular lattices, Phys. Rev. B **97**, 125430 (2018).

[44] J. Y. Zhang, B. Zhao, T. Zhou, Y. Xue, Y. Fang, C. L. Ma, and Z. Q. Yang, Topologically trivial states induced by strong spin-orbit coupling and Chern insulators in doped $X(C_{21}N_3H_{15})$ (X = Ta, Hf) metal-organic frameworks, Phys. Rev. B **99**, 035409 (2019).

[45] Y. Li, J. Y. Zhang, B. Zhao, Y. Xue, and Z. Q. Yang, Constructive coupling effect of topological states and topological phase transitions in plumbene, Phys. Rev. B **99**, 195402 (2019).

[46] P. E. Blöchl, Phys. Rev. B **50**, 17953 (1994).

[47] G. Kresse and J. Furthmüller, Efficient iterative schemes for *ab initio* total-energy calculations using a plane-wave basis set, Phys. Rev. B **54**, 11169 (1996).

[48] J. P. Perdew, K. Burke, and M. Ernzerhof, Generalized Gradient Approximation Made Simple, Phys. Rev. Lett. **77**, 3865 (1996).

[49] S. L. Dudarev, G. A. Botton, S. Y. Savrasov, C. J. Humphreys, and A. P. Sutton, Electron-energy-loss spectra and the structural stability of nickel oxide: An LSDA+U study, Phys. Rev. B **57**, 1505 (1998).

[50] A. Togo, F. Oba, and I. Tanaka, First-principles calculations of the ferroelastic transition between rutile-type and $CaCl_2$-type SiO_2 at high pressures, Phys. Rev. B **78**, 134106 (2008).

[51] N. Marzari and D. Vanderbilt, Maximally localized generalized Wannier functions for composite energy bands, Phys. Rev. B **56**, 12847 (1997).

[52] I. Souza, N. Marzari, and D. Vanderbilt, Maximally localized Wannier functions for entangled energy bands, Phys. Rev. B **65**, 035109 (2001).

[53] A. A. Mostofi, J. R. Yates, Y. S. Lee, I. Souza, D. Vanderbilt, and N. Marzari, Wannier90: A tool for obtaining maximally localized Wannier functions, Comput. Phys. Commun. **178**, 685 (2008).

[54] X. J. Wang, J. R. Yates, I. Souza, and D. Vanderbilt, *Ab initio* calculation of the anomalous Hall conductivity by Wannier interpolation, Phys. Rev. B **74**, 195118 (2006).

[55] Q. S. Wu, S. Zhang, H. F. Song, M. Troyer, and A. A. Soluyanov, WannierTools: An open-source software package for novel topological materials, Comput. Phys. Commun. **224**, 405 (2018).

[56] K. Haeuseler and S. K. Srivastava, Phase equilibria and layered phases in the systems A_2X_3-M_2X_3-$M'X$ (A = Ga, In; M = trivalent metal; M' = divalent metal; X = S, Se), Z. Kristallogr. **215**, 205 (2000).

[57] See Supplemental Material at http://link.aps.org/supplemental/10.1103/PhysRevB.107.085416 for detailed information about the structural, magnetic configurations, band structures, strain effect, and carrier doping effect of the monolayer TM-Al_2S_4 (TM = Mn, Fe, Cr, V); the structural, magnetic configurations, and band structures of the bulk TM-Al_2S_4(TM = Mn, Fe, Cr, V, Ni); the energy difference ΔE of monolayer $NiAl_2S_4$ as a function of effective Hubbard U; the phase diagram of global

band gap for monolayer $NiAl_2S_4$ with respect to strain; and the band structures of monolayer $NiAl_2S_4$ with collinear AFM and FM states.

[58] J. B. Goodenough, Theory of the role of covalence in the perovskite-type manganites [La, M(II)]MnO_3, Phys. Rev. **100**, 564 (1955).

[59] J. B. Goodenough, An interpretation of the magnetic properties of the perovskite-type mixed crystals, J. Phys. Chem. Solids **6**, 287 (1958).

[60] H. Yuan, H. Shimotani, A. Tsukazaki, A. Ohtomo, M. Kawasaki, and Y. Iwasa, High-density carrier accumulation in ZnO field-effect transistors gated by electric double layers of ionic liquids, Adv. Funct. Mater. **19**, 1046 (2009).

[61] A. S. Dhoot, C. Israel, X. Moya, N. D. Mathur, and R. H. Friend, Large Electric Field Effect in Electrolyte-Gated Manganites, Phys. Rev. Lett. **102**, 136402 (2009).

[62] Y. Xue, J. Y. Zhang, B. Zhao, X. Y. Wei, and Z. Q. Yang, Non-Dirac Chern insulators with large band gaps and spin-polarized edge states, Nanoscale **10**, 8569 (2018).

[63] J. Y. Zhang and C. L. Ma, Room-temperature non-Dirac quantum anomalous Hall states, half semiconductors, and strain-tuned half metals in monolayer zirconium trihalide, Phys. Rev. B **104**, 205429 (2021).

[64] D. J. Thouless, M. Kohmoto, M. P. Nightingale, and M. den Nijs, Quantized Hall Conductance in a Two-Dimensional Periodic Potential, Phys. Rev. Lett. **49**, 405 (1982).

[65] Y. G. Yao, L. Kleinman, A. H. MacDonald, J. Sinova, T. Jungwirth, D. S. Wang, E. Wang, and Q. Niu, First Principles Calculation of Anomalous Hall Conductivity in Ferromagnetic bcc Fe, Phys. Rev. Lett. **92**, 037204 (2004).